

---

# Attosecond photoemission from isolated nanoparticles in strong laser fields

Philipp Rupp

---



München 2014



---

# **Attosekunden Photoemission von isolierten Nanopartikeln in starken Laserfeldern**

**Philipp Rupp**

---

Masterarbeit  
an der Fakultät für Physik  
der Ludwig-Maximilians-Universität  
München

vorgelegt von  
Philipp Rupp  
aus Aalen

Gutachter: Prof. Dr. Matthias Kling

München, den 16.06.2014



# Abstract

This work covers two parts of the attosecond physics of nanoparticles, namely photoemission of electrons from nanoparticles interacting with few-cycle pulses in the strong-field regime and attosecond streaking of the nanoparticles in laser pulses in the visible/infrared (VIS/IR) spectral range.

The photoemitted electrons are recorded by single-shot velocity-map imaging and simultaneous carrier-envelope phase tagging. This provides a two-dimensional final electron momentum distribution, correlated with the waveform of the 5 fs pulse. The measurements are performed at an intensity range of  $1\text{--}5 \times 10^{13} \frac{\text{W}}{\text{cm}^2}$  which covers the region of quasistatic tunneling of the emitted photoelectron at high intensities and non-adiabatic tunneling at intermediate intensities. Numerical simulations have been performed that reproduce the main features of the photoemission spectrum. A modification of the quasistatic tunneling was used in the simulation model and provides insight into the exact mechanisms that play a role in strong fields. The studied mechanisms include the ionization process and field enhancements around the dielectric nanoparticles. The high cutoff energies of the electrons can only be explained by rescattering on the particle itself and meanfield effects. A study of different materials demonstrates the influence of the ionization potentials and permittivities on the final momentum distribution. The results obtained help us gain insight into the ionization process of solids in strong fields.

An analysis of the temporal features of the nanoparticle ionization process is performed by attosecond streaking. The pump-probe experiment uses 205 as XUV pulses and few-cycle VIS/IR pulses to trigger the ionization and acceleration of electrons, respectively. The resulting electron energies are recorded by a time-of-flight (TOF) spectrometer. In contrast to gas streaking the high energy electrons from nanoparticles show a behavior that is shifted in time. Our simulations suggest that this shift can be attributed to the electron paths with a longer propagation time inside the particle. A longer path leads to a delayed exit time at the surface and is directly correlated to a higher probability of elastic scattering. Since inelastic scattering is found to be a limiting factor of the path length it determines the maximum shift measured in the cutoff region. The measurements show that the inelastic mean free path is significantly longer in the experiment than expected before.



# Zusammenfassung

Diese Arbeit befasst sich mit zwei Aspekten der Attosekundenphysik von Nanopartikeln, zum einen mit der Photoemission von Elektronen aus Nanopartikeln im Starkfeld von Wenig-Zyklen-Laserpulsen und zum anderen mit dem Attosekunden-Streaking solcher Partikel mit Laserpulsen im sichtbaren und infraroten Spektralbereich.

Die Erfassung der photoemittierten Elektronen erfolgt durch Einzelschuss-Aufnahmen der projizierten Geschwindigkeitsverteilung und der gleichzeitigen Messung der Träger-Einhüllenden-Phase. Auf diese Weise können die Elektronengeschwindigkeiten direkt mit dem Feldverlauf des 5 fs Pulses in Verbindung gebracht werden. Die Messungen werden für Intensitäten von  $1\text{-}5 \times 10^{13} \frac{\text{W}}{\text{cm}^2}$  durchgeführt. Da dies auch Tunnelionization im nicht-adiabatischen Bereich beinhaltet, wird das quasistatische Tunnelmodell in den Simulationen modifiziert. Die Simulationen geben die Hauptmerkmale des Photoemissionsspektrums wieder und klären die genauen Mechanismen in starken Feldern. Zusätzlich zum Ionisationsprozess wird auch die Feldverstärkung rund um die dielektrischen Nanopartikel untersucht. Die hohen Cutoff-Energien der Elektronen können nur mittels Rückstreuung an den Nanopartikeln selbst und durch Wechselwirkung mit den anderen Elektronen erklärt werden. Verschiedene Materialien verdeutlichen den Einfluss des Ionisationspotentials und der Permittivität auf die finale Impulsverteilung der Elektronen. Die durchgeführten Versuche an Festkörpern führen zu einem besseren Verständnis der Ionisationsprozesse in starken Feldern.

Attosekunden Streaking erlaubt die Untersuchung der zeitlichen Abläufe innerhalb der Nanopartikel. Dabei werden VIS/IR-Pulse mit wenigen Zyklen und 250 as XUV-Pulse verwendet, um Elektronen zu ionisieren und die anschließende Beschleunigung zu beobachten. Die Bestimmung der Elektronenenergien erfolgt mittels eines Flugzeitspektrometers. Im Gegensatz zum Gasstreaking zeigen die hochenergetischen Elektronen von Nanopartikeln ein zeitlich versetztes Verhalten. Es konnte durch entsprechende Simulationen gezeigt werden, dass die Emissionstiefe von bis zu  $10 \text{ \AA}$  und die damit verbundene längere zurückgelegte Wegstrecke im Teilchen diese Verzögerung verursacht. Die größere Wegstrecke führt zu einem verspäteten Austritt der Elektronen aus der Nanoteilchenoberfläche und erhöht gleichzeitig die Wahrscheinlichkeit einer elastischen Streuung. Gleichzeitig limitiert die inelastische Streuung den maximalen gemessenen Versatz im Experiment. Der direkte Vergleich von Experiment und Simulation zeigt, dass die inelastische freie Weglänge größer sein muss, als in der Literatur angenommen.



# Contents

Abstract	v
Zusammenfassung	vii
<b>1 Introduction</b>	<b>1</b>
<b>2 Theory</b>	<b>5</b>
2.1 Ultrashort laser pulses . . . . .	5
2.2 Mie-theory . . . . .	6
2.3 Strong-Field photoemission . . . . .	6
2.3.1 Multiphoton ionization . . . . .	7
2.3.2 Tunnel ionization . . . . .	7
2.4 Attosecond streaking . . . . .	9
<b>3 Simulations</b>	<b>11</b>
3.1 Description . . . . .	11
3.2 Modification . . . . .	14
3.3 Simulating attosecond streaking . . . . .	16
<b>4 Experimental Setup</b>	<b>19</b>
4.1 Generation of few-cycle laser pulses . . . . .	19
4.2 Single-shot phase-tagged VMI . . . . .	21
4.3 Interferometric attosecond streaking setup . . . . .	24
4.4 Sample preparation . . . . .	25
<b>5 Photoemission from nanoparticles in strong IR-fields</b>	<b>27</b>
5.1 Methods . . . . .	27
5.2 Experimental results from SiO <sub>2</sub> nanoparticles . . . . .	30
5.3 Simulations . . . . .	36
5.4 Comparison between experiment and simulation . . . . .	38
5.5 Results from different materials . . . . .	42
5.6 Conclusion . . . . .	45

<b>6</b>	<b>Attosecond streaking on isolated nanoparticles</b>	<b>47</b>
6.1	Methods . . . . .	47
6.2	Experimental results from SiO <sub>2</sub> streaking . . . . .	50
6.3	Comparison of experimental results with simulations . . . . .	54
6.4	Conclusion . . . . .	59
<b>7</b>	<b>Conclusion and outlook</b>	<b>61</b>
	<b>Bibliography</b>	<b>63</b>
	<b>Acknowledgements</b>	<b>67</b>

# Chapter 1

## Introduction

In our daily life we experience events with very different timescales. Time spent in school might seem very long, time playing with friends passes by incomparably faster but both have in common that everybody has some imagination about periods like seconds, hours or years. Today, however, it is possible to measure processes with a time resolution down to attoseconds ( $1 \text{ as} = 10^{-18} \text{ s}$ ). This opens up the possibility to resolve the motion of electrons which takes place on the attosecond timescale.

The ability to measure shorter and shorter time periods can be closely related to the breakthroughs in ultra-fast optics (figure 1.1). The invention of the laser in 1960 [1] and the progress of nonlinear optics [2] paved the way to ultra-fast optics and are of fundamental importance in today's time-resolved experiments [3]. Since the advent of femtosecond ( $1 \text{ fs} = 10^{-15} \text{ s}$ ) lasers it is possible to monitor chemical reactions by the observation of nuclei. For this work Ahmed Zewail was awarded with the Nobel prize in chemistry in 1999 [4]. The lower limit for time resolved measurements remained in the low fs-regime for some time until the end of the 20th century.

In the following decade the generation of single attosecond pulses by High Harmonic Generation (HHG) lowered the reachable time resolutions to the attosecond regime. Not only atomic motion can be made visible but also the movement of electrons in atoms or condensed matter [6].

A comparison of the shortest detectable processes in optics with electronic switching times (blue curve) is shown in figure 1.1. Since about 10 years the clock rate in integrated circuits is limited to about 3 GHz due to the charging time of the connectors. By using optical signals to change the material properties on an attosecond timescale, this restraint can in principle be overcome. Using light waves and dielectrics as switches is a vision for the future realization of electronics in the petahertz regime [5]. For a significant change of properties in such materials strong fields in the intensity regime above  $10^{13} \frac{\text{W}}{\text{cm}^2}$  are required

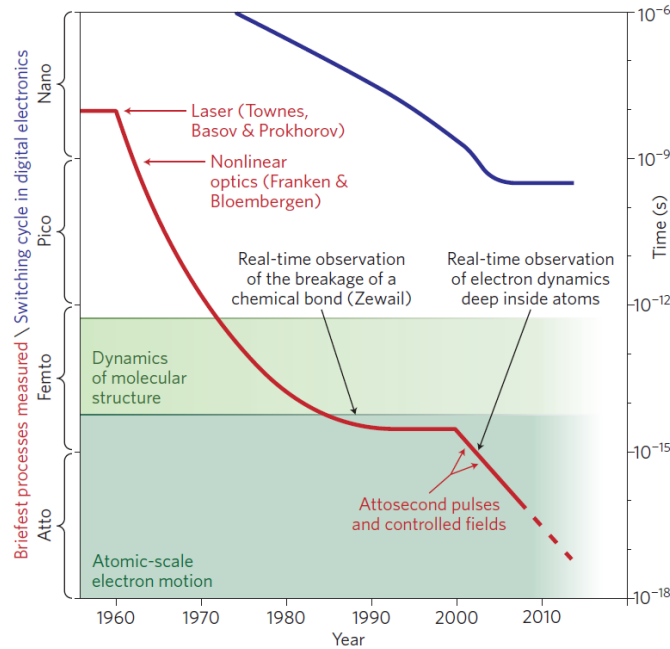


Figure 1.1: Timescales in science and digital electronics. The red curve shows the shortest timescales that are accessible by ultrafast optical laser pulses together with the most important steps that were made during the improvement of time resolution. The blue line shows the evolution of the realized clock rates in digital electronics. Taken from [5].

and a detailed understanding of the interaction with matter is needed.

In the past much research on strong-field interaction with atoms or molecules has been done [7, 8]. The ionization mechanism has been described in detail for those systems [9] but the interaction with solid state materials and their more complex potential landscapes are still to be investigated, especially in the intermediate regime between multiphoton and tunnel ionization.

Nanosystems are well-suited model systems to study solid state physics, since they have well-defined properties like size, shape and electric permittivity. The interaction of spherical particles with electric fields in free space can be modeled by numerical simulations and compared to experimental results. Nanoparticles can be used to form a nanoplasma by ionization with laser pulses, allowing the study of laser-plasma interaction [10]. A second laser pulse delayed by some picoseconds can be used to create shockwaves in the plasma that lead to the emission of monoenergetic ion bursts.

This work will concentrate on the timescale below five femtoseconds where atoms or residual ions can be treated as fixed and solely electronic motions are investigated. The acceleration of photoemitted electrons can be used to study the near-field distribution

around nanoparticles and investigate the rescattering process of those electrons [11, 12]. Photoemitted electrons that are driven back to the nanoparticle by the electric laser field can reach very high kinetic energies around one order of magnitude higher than for a similar process in gas targets. Attosecond streaking experiments performed on isolated nanoparticles provide insight into the scattering probabilities and timings inside dielectrics.

The remainder of this thesis is organized as follows. Chapter 2 explains the theoretical background of this work and chapter 3 deals with the theoretical model used in the simulations. Chapter 4 describes the experimental setup. Chapter 5 concerns the experiments about strong-field photoemission from nanoparticles and chapter 6 describes first attosecond streaking experiments with  $\text{SiO}_2$  nanoparticles. A conclusion is drawn in chapter 7.



# Chapter 2

## Theory

### 2.1 Ultrashort laser pulses

Since the emergence of mode locking in Ti:sapphire lasers ultrashort laser pulses with pulse duration in the femtosecond regime are routinely used. The electric field of a linearly polarized pulses with carrier frequency  $\omega_L$  can be approximated by

$$\vec{E}(x, t) = E_0 \exp(-2 \ln 2 (t/\sigma)^2) \cos(\omega_L(t - x/c) + \phi_0) \vec{e}_z. \quad (2.1)$$

$\sigma$  denotes the FWHM<sup>1</sup>-pulse duration and  $\phi_0$  the carrier-envelope phase (CEP). For multi-cycle pulses ( $\sigma \gg \omega_L^{-1} = \frac{T}{2\pi}$ ) the CEP does not play a noticeable role because the envelope doesn't change substantially during one cycle of the electric field. Only for few cycle pulses different CEPs result in distinguishable waveforms. For  $\phi_0 = 0$  the electric field is shaped like a cosine-function and thus the peak intensity is reached at the peak of the envelope, while for  $\phi_0 = \frac{\pi}{2}$  the waveform is sine-like resulting in a pulse reaching two (slightly lower) intensity peaks right before and after the envelope peak.

In order to generate few-cycle pulses a broad spectrum is necessary to provide the short laser pulse durations. A Fourier transformation of the temporal evolution (equation 2.1) shows the condition for the FWHM-bandwidth in the frequency domain  $\Delta\nu$ :

$$\sigma \cdot \Delta\nu = 0.44 \quad (2.2)$$

This demands for a bandwidth of at least 140 nm (FWHM) for a 5 fs pulse at 700 nm. Since this is only true for perfectly Gaussian shaped pulses with an absolutely flat spectral phase (i.e. no chirp) the spectrum for the generation of such few-cycle-pulses should be broader than 140 nm.

---

<sup>1</sup>Full-Width-Half-Maximum

## 2.2 Mie-theory

Solving Maxwell's equations for arbitrary geometries and incident beams is analytically impossible in most cases and also numerically challenging (see for example [13, 14] for FDTD integrators). The problem of a spherical particle illuminated by a plane wave however was solved almost 100 years ago by Gustav Mie [15]. Similar to the (scalar) Laplace's spherical harmonics that arise for example when solving the hydrogen atom, Mie introduced vector spherical harmonics (VSH) and a size parameter  $\chi$  defined as

$$\chi = \frac{2\pi r}{\lambda}, \quad (2.3)$$

depending on the wavelength  $\lambda$  of the incoming wave and the radius  $r$  of the sphere. Using  $\chi$  and the permittivity  $\epsilon$  of the material, the incoming wave can be decomposed into a infinite series of VSH. The hereby calculated Mie coefficients in turn give the internal as well as the scattered field in and around the particle. In case of incoming plane waves  $\vec{E}_{\text{in}} = E_0 \cos(\omega t - kx)\vec{z}$  (or Gaussian beam profiles) the lower-order Mie coefficients are sufficient to describe the problem with good accuracy. Especially in case of  $\chi \ll 1$ , that is particles much smaller than the wavelength, it is sufficient to consider the first order Mie coefficient which describes an induced dipole in the particle due to polarization effects. This approximation is called Rayleigh scattering. The resulting potentials (without time dependence) are

$$\Phi = \begin{cases} -\frac{3}{\epsilon + 2}E_0z & r < a \\ -E_0z + \frac{\epsilon - 1}{\epsilon + 2}E_0\frac{a^3}{r^3}z & r \geq a. \end{cases} \quad (2.4)$$

The field enhancement on the  $z$ -axis right above the surface of dielectric particles is

$$\alpha = \frac{|\vec{E}|}{E_0} = \frac{|-\nabla\Phi|}{E_0} = \frac{3\epsilon}{\epsilon + 2}. \quad (2.5)$$

In the simulation model used here the fields are calculated by the full Mie-solution or dipole approximation depending on the particle size.

## 2.3 Strong-Field photoemission

In 1965, L.V. Keldysh presented a theory about ionization of atoms with an ionization potential  $I_p$  [7]. The atom interacts with a laser fields with a peak electric fields  $E_0$  and an angular frequency  $\omega_L$ . Two regimes can be distinguished by the Keldysh parameter

$$\gamma = \sqrt{\frac{I_p}{2U_p}} = \frac{\omega_L\sqrt{2mI_p}}{eE_0} \quad (2.6)$$

that relates the ionization potential to the ponderomotive potential  $U_p$  – defined as the averaged quiver energy of an electron in an electric field:

$$U_p = \frac{e^2 E_0^2}{4m\omega_L^2}. \quad (2.7)$$

For  $\gamma \gg 1$  multiphoton ionization is the dominant process while for  $\gamma \ll 1$  tunnel ionization describes the effects best.

Those formulas are equivalent to a comparison of laser frequency to "tunneling time"  $\omega_t^{-1}$  of the electron with mass  $m$  (defined in [7]). The ionization rate can also be derived for static fields which means  $\omega_L \ll \omega_t$  or  $\gamma \ll 1$ . Because the electric field does not change drastically during the tunneling of the electron this is also called quasistatic tunneling. For the case of comparable tunneling time and laser period, tunneling is still dominant but a modification to the ionization rate is necessary as described in section 3.2. Because of the significant tunneling time (compared to the laser period) the electric field is changing during the ionization process – denoting this modification as non-adiabatic.

In the other limiting case represented by  $\omega_L \gg \omega_t$  or  $\gamma \gg 1$  the ionization process can be better understood in the photon picture. The atom absorbs several photons with an total energy above the ionization potential resulting in one released electron.

### 2.3.1 Multiphoton ionization

For  $\gamma \gg 1$  the ionization process is best described by multiple absorptions of photons with an energy of well below  $I_p$  each (see figure 2.1a). In this case the whole process can be treated by perturbation theory. The ionization rate depends on the intensity as

$$\Gamma \propto I^n. \quad (2.8)$$

For sufficiently high enough intensities more photons than necessary can be absorbed which is known as above-threshold ionization (ATI) [16]. In the electron spectra peaks with a separation of  $\hbar\omega_L$  can be detected.

### 2.3.2 Tunnel ionization

For electric fields of similar strength as the atomic fields the Coulomb potential can be distorted by the laser pulse and perturbation theory can no longer be applied (see figure 2.1a). The classic wave picture of light is then more appropriate than a description with photons. The atomic potential is bent in such a way that the electron can tunnel through the barrier and reach the continuum at rest. The quasistatic ionization rate is described by the ADK

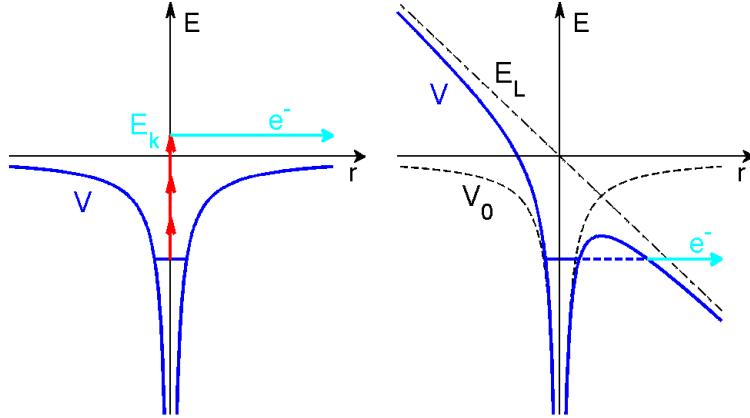


Figure 2.1: Illustration of possible ionization mechanism. a) Multiphoton ionization by three photons leads to one electron (cyan). Electric laser field is weak compared to atomic potential (blue). b) Tunnel ionization occurs for electric fields  $E_L$  that "bend" the atomic potential during one half-cycle. The electron has a probability to tunnel through the remaining barrier (dashed line).

theory (named after Ammosov, Delone and Krainov [17]). After ionization the electrons can then be described classically by following Newton's laws in the electric laser field. Due to the oscillating nature of laser fields the electrons can be driven back and perform several processes of which two are of high importance to this work. The recollision with the parent ion leads to high energy electrons with a cutoff energy of [18]

$$E_c = 10.007U_p + 0.538I_p. \quad (2.9)$$

This process can also be observed for nanoparticles in a similar way which will be discussed in chapter 5.

On the other hand, recombination can transfer the kinetic energy of the electrons to high energy photons in the extreme ultraviolet (XUV) regime. The XUV-spectrum shows a similar cutoff than the rescattered electrons at the energy  $E_c$ :

$$E_c = I_p + 3.17U_p. \quad (2.10)$$

This mechanism is known as the three-step model, consisting of ionization, acceleration in the laser field and recombination. When using very short pulses ( $\sim 5$  fs) the whole process only takes place during one half-cycle of the laser pulse. This leads to a XUV-continuum and can be used for time-resolved measurements in the attosecond regime (chapter 6).

In principle the concept of tunnel ionization can be extended to even larger intensities and fields. Very strong fields can lead to a bending condition that allows some electrons to

overcome the atomic potential barrier without tunneling. This is called over-the-barrier-ionization but is not reached by the intensities used in this work.

## 2.4 Attosecond streaking

The attosecond streak camera is suited for resolving very fast processes like chemical reactions, propagation of light or charge carrier movements [19]. The original streak camera (see figure 2.2a) uses a photocathode to generate electrons out of a time dependent optical pulse (cyan) that is to be measured. The generated electrons are deflected by an applied electrical field that is changing its magnitude with time. The time dependent signal can then be retrieved by the electron detection on a screen. The information from the temporal domain is transferred to a spatial dimension. Typically resolutions of down to 100 fs can be reached by controlling the deflecting fields electronically.

With attosecond pulses much shorter processes on the timescale below one femtosecond can be resolved. Since those timescales can not be reached with electronically switched deflection another even faster process is necessary. Attosecond streaking applies the varying electric field in an optical laser pulse itself [21].

Electrons are emitted during a certain period in the driving laser field cycle (see figure 2.2b, red curve). In this work a single 250 as XUV and a CEP-stable VIS/IR pulse with controllable delay between the two pulses are used (details of the setup will be described in chapter 4.3). The initial electron energy is coded with colors (blue to red, high to low energies) to visualize the effect of chirp. The average initial electron energy (green) doesn't experience any change of velocity (born at the zero crossing of the vector potential). The black line indicates the initial energy distribution right after emission. The black peak on the right illustrates the retrieved spectrum in absence of any streaking field. In case of a streaking field the electrons experience a change of velocity proportional to the grey vector potential. The final electron velocity is denoted as the green arrow which translates to the green spectrum on the right. In case of a rising vector potential (upper image) the chirp is compensated by the streaking leading to a narrow spectrum, a falling vector potential (lower image) broadens the final electron velocity distribution. The final electron spectrum is detected and energetically resolved by a time-of-flight (TOF) spectrometer.

Attosecond streaking is frequently done with gas samples. This work will present the streaking of nanoparticles which includes additional processes like field enhancement that do not occur for atoms.

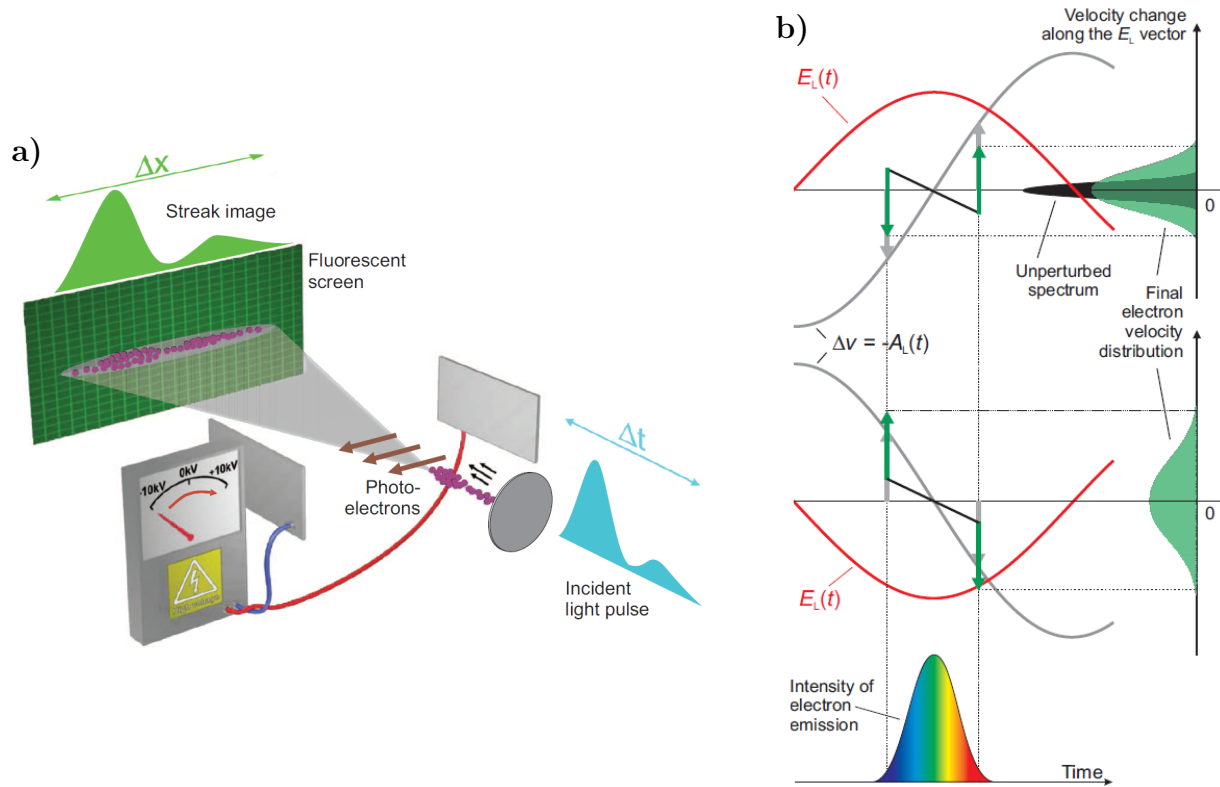


Figure 2.2: a) Principle of a streak camera. The incident pulse has some temporal profile that is resolved. The cathode emits photoelectrons that are deflected by a varying electric field. The temporal signature is translated into spatial information on a fluorescent screen. The resolution is limited by the slope of the voltage change. b) Attosecond streaking: The initial (chirped) electron emission is shown in colors on the bottom and streaked due to an electric field (red). The final velocity distribution is shown on the right (green). A detailed description can be found in the text. Both figures are taken from [20].

# Chapter 3

## Simulations

### 3.1 Description

For the simulation of the photoionization process and further propagation of electrons the M<sup>3</sup>C-Code was used [11]. This name stands for a **M**ie-field solution, **m**eanfield contribution, **M**onte-Carlo-simulation. For given input parameters like nanoparticle and laser pulse properties this code simulates electron and field dynamics induced by the laser field. The positions and momenta of all free electrons can be retrieved and the two-dimensional projection can be compared to the experiments (see section 4.2). From that we would like to understand how, where and when the electrons are ionized, what kind of influence they experience during their propagation and how material properties affect those processes.

The electric field around the spherical particle is obtained by the plane wave solution decomposed into several frequencies in order to assemble the few-cycle-pulse (see section 2). For particles much smaller than the wavelength of the laser field this solution is similar to a dipole oscillation but for larger nanoparticles a difference can be seen: The maximum field enhancement shifts from the poles towards the backside of the particle. This means the front-/back-symmetry in the propagation direction is not conserved anymore. The temporal shape  $f(t) \cdot E_0 \cos(\omega_L(t - \frac{x}{c}) + \phi_0) \vec{e}_z$  consists of a fast oscillating sinusoidal with the carrier frequency  $\omega_L$  and the carrier-envelope-phase  $\phi_0$  and a Gaussian envelope  $f(t) = \exp\left(-2 \ln 2 \left(\frac{t}{\sigma}\right)^2\right)$  with intensity duration  $\sigma$  (FWHM). The simulation was done for several carrier envelope phases and thus the phase dependence of the final electron momenta can be retrieved from the simulations.

The ionization process itself is simulated by a Monte-Carlo method incorporating 1000 probing positions on the particle surface. At those randomly distributed points located all over the particle surface the ionization probability is calculated every 0.1 as. For the quasistatic tunneling the probability is a function of the ionization potential and the

absolute value of the electric field (at each position). The exact mechanism (tunneling versus multiphoton ionization) is investigated in chapter 3.2. The newly "born" electrons are positioned at the calculated tunneling exit at rest and then follow classical trajectories calculated by a Verlet algorithm with 10 as step size. Because this stochastic process would describe only some thousands of electrons per nanoparticle one electron is represented by several hundreds of trajectories which increases the statistical value. In addition to the dielectric Mie-field around the nanoparticle all charged particles interact with each other which would make numerical calculations almost impossible due to the required computation time. Therefore the electric fields from all charged particles (residual ions in the nanoparticle and electrons) are summed up and expanded into a multipole series. The first 4–10 orders were used in the meanfield calculations to describe the interaction between all charges.

For electrons inside the particle two kind of scattering processes are implemented in the model: First, elastic scattering without any change of kinetic energy and second inelastic scattering which leads to ionization of secondary electrons. Elastic scattering changes the direction of the electron isotropically but doesn't further influence the particle. This process is determined by the energy-dependent (elastic) mean free path

$$l_{\text{mfp}} = l_0 + l_1 \cdot E_k + l_2 \cdot E_k^2 \quad (3.1)$$

with kinetic energy  $E_k$  and the material specific parameters  $l_0, l_1$  and  $l_2$ . For  $\text{SiO}_2$  the parameters were extracted from experimental data for elastic scattering giving the values  $l_0 = 2.0 \text{ \AA}$ ,  $l_1 = 0.053 \frac{\text{\AA}}{\text{eV}}$  and  $l_2 = 0.00018 \frac{\text{\AA}}{\text{eV}^2}$  [22]. In our range of kinetic energies this gives a  $l_{\text{mfp}}$  of about 2–3.5  $\text{\AA}$  which was also used for the other investigated materials due to similar atomic weights and material densities [23].

Second, inelastic scattering is possible with a certain probability if the kinetic energy of an electron is larger than the ionization potential  $I_p$  of the material. The electron inside the nanoparticle then loses the energy  $I_p$  and ionizes another electron (but does not change its direction). The inelastic cross section  $\sigma$  is described by the Lotz-formula which was derived for atoms but can be used when taking into account the number density of the material [24, 25]:

$$\sigma = a \frac{\ln(E_k/I_p)}{E_k I_p} \text{ with } a = 4.5 \times 10^{-14} \text{ cm}^2 (\text{eV})^2. \quad (3.2)$$

The ionization mechanism itself plays an important role in this model because it determines where and when electrons are "born" and are able to further propagate. In this context "born" means that a so-far bound electron is ionized either by an electric field

or other electrons and is now able to freely propagate. For small Keldysh parameters  $\gamma = \sqrt{\frac{I_p}{2U_p}} \ll 1$ , i.e. high intensities (for given  $I_p$ ), tunnel ionization is the most important mechanism [7]. The ionization rate only depends on the *instantaneous* electric field and is highly nonlinear (since the probability depends exponentially on the inverse of the tunnel barrier integral). So for an idealized sinusoidal wave the ionization rate is tightly confined around the peaks of the field which leads to separated electron bursts. Those bursts are alternatively emitted in the directions of the two poles depending on the sign of the electrical field. Only at positions where the radial component  $\vec{E}_r$  points inside the particle the negatively charged electron is pulled outside.

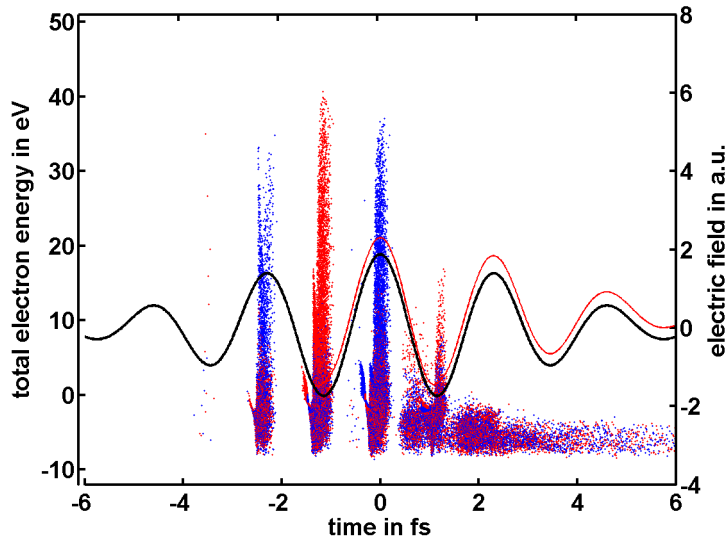


Figure 3.1: Birth time of electrons with certain energies. Black: dielectric Mie-field at the pole for a 5 fs laser pulse at 700 nm. Red: Total field at the same pole including meanfield. Simulations were carried out for a 100 nm  $\text{SiO}_2$  particle at an intensity of  $2 \times 10^{13} \frac{\text{W}}{\text{cm}^2}$ . Each dot represents an electron that is born at a certain time. The position on the  $y$ -axis corresponds to the total energy (kinetic plus potential) after 30 fs. The color indicates the direction of emission: red means upwards (positive  $z$ ), blue downwards (negative  $z$ ).

In figure 3.1 the red and blue distributions show when exactly electrons are emitted. This happens not only at the peak of the field (black) but already during the rising edge. The electrons generated during this rising edge contribute to the (counteracting) meanfield distorting the resulting total field.

To compare the simulations to the experimental results only the electrons that would reach the detector in the experiment are considered for the final momentum distribution. After the interaction with the laser field the nanoparticle is charged up and generates an

electric potential. Since this residual potential is attractive for photoemitted electrons it is called a trapping potential. Only electrons with a sufficiently high kinetic energy can overcome this barrier and can finally be detected by the VMI. The ones that are still inside the particle or do not have enough kinetic energy are neglected. This evaluation is made 15 fs after the laser peak. In figure 3.1 different kinds of electron trajectories can be identified. The thin line at the rising edge of each half-cycle at a few eV can be assigned to *direct* electrons that just follow the electric field after being emitted and do not experience any collision with the nanoparticle. The greater portion emitted later are *rescattered* electrons that are driven by the field into the continuum and back to the particle and scatter one or more times. This exact mechanism allows electrons to gain the highest energies in the cutoff region. Electrons generated by impact ionization are less probable but can happen later in the laser cycle.

## 3.2 Modification of ionization model

For smaller laser intensities when  $U_p$  becomes comparable or smaller than  $I_p$ , the electric field can not be treated as static anymore during the tunneling time  $\omega_t^{-1}$ . The description by static tunnel ionization will not be correct and modifications to the model have to be considered. In our typical regime of the incident laser field intensity of  $1 \times 10^{13} \frac{\text{W}}{\text{cm}^2}$  the Keldysh parameter  $\gamma$  for the field at the surface of the particle is on the order of 1.5 considering the enhancement of the dielectric field at the surface of the particle. Theoretical studies [26] show that the tunneling model itself can still be used but the ionization rate has to be modified. The time-dependent Keldysh parameter becomes  $\gamma(t) = \gamma/f(t)$  and the phase reads  $\theta(t) = \omega_L t + \phi_0 - \pi k$  with  $k \in \mathbb{Z}, \theta \in [-\frac{\pi}{2}, -\frac{\pi}{2}]$ . So the ionization rate for non-adiabatic tunnel ionization becomes

$$\Gamma(t) = A_{n^*,0} \left( \frac{3\kappa}{\gamma^3} \right)^{1/2} C I_p \left( \frac{2(2I_p)^{3/2}}{E_0 f(t)} \right)^{2n^*-1} \exp \left( -\frac{E_0^2 f^2(t)}{\omega_L^3} \Phi(\gamma, \theta) \right). \quad (3.3)$$

The subcycle dependence is only important in the exponential factor which determines the timing of ionization. The function  $\Phi$  is given by

$$\Phi(\gamma, \theta) = \left( \gamma^2 + \sin^2 \theta + \frac{1}{2} \right) \ln c - \frac{3\sqrt{b-a}}{2\sqrt{2}} \sin |\theta| - \frac{\sqrt{b+a}}{2\sqrt{2}} \gamma \quad (3.4)$$

and includes the following variables

$$a = 1 + \gamma^2 - \sin^2 \theta, \quad b = \sqrt{a^2 + 4\gamma^2 \sin^2 \theta}, \quad (3.5)$$

$$c = \sqrt{\left(\sqrt{\frac{b+a}{2}} + \gamma\right)^2 + \left(\sqrt{\frac{b-a}{2}} + \sin|\theta|\right)^2}. \quad (3.6)$$

All other pre-exponential terms make sure that the total rate matches the cycle-averaged results. Since the rates are derived from atomic ionization models they include the effective principal quantum number

$$n^* = \frac{1}{\sqrt{2I_p[\text{eV}]}} \quad (3.7)$$

and coefficients from radial parts of the wave function

$$A_{n^*,0} = \frac{2^{2n^*}}{n^* \Gamma(n^* + 1) \Gamma(n^*)}. \quad (3.8)$$

The Perelemov-Popov-Terent'ev (PPT) correction to the quasistatic limit is expressed by  $C$  and approximated by

$$C \approx e^{-0.1\gamma} \quad (3.9)$$

while  $\kappa$  is defined as

$$\kappa = \ln(\gamma + \sqrt{\gamma^2 + 1}) - \frac{\gamma}{\sqrt{\gamma^2 + 1}}. \quad (3.10)$$

As can be seen from the expressions above not only the instantaneous electric field affects the ionization rate but also the phase  $\theta$  and therefore the envelope  $f(t)$ . The field enhancement only has a scaling effect on the fields and because of the relatively low intensities the meanfields are rather weak and only lead to small distortions of the laser waveform. Therefore we assume that the total field  $E_{\text{total}}$  is still in similar shape than the driving laser field  $E_L$  and use this for calculating the envelope of the electric field. In the simulation the phase  $\theta$  is assumed to be the same for the laser field and the total field and thus the envelope can be calculated by using

$$\frac{f_L(t)}{E_L(t)} = \frac{f_{\text{total}}(t)}{E_{\text{total}}(t)}. \quad (3.11)$$

Figure 3.2a compares the time dependence of the ionization yield of the modified tunneling model to the quasistatic tunneling regime. Instead of a strong  $\theta$  dependence during one cycle in the tunneling regime (Figure 3.2a (blue)) now there also is a phase independent contribution which leads to ionization during the whole laser pulse envelope (green). The phase independent ionization leads to a totally different behavior in the low-intensity regime and has a large influence on the highest energy electrons. Compared to the quasistatic limit the electrons are spread out more over time (figure 3.2b). This leads to a

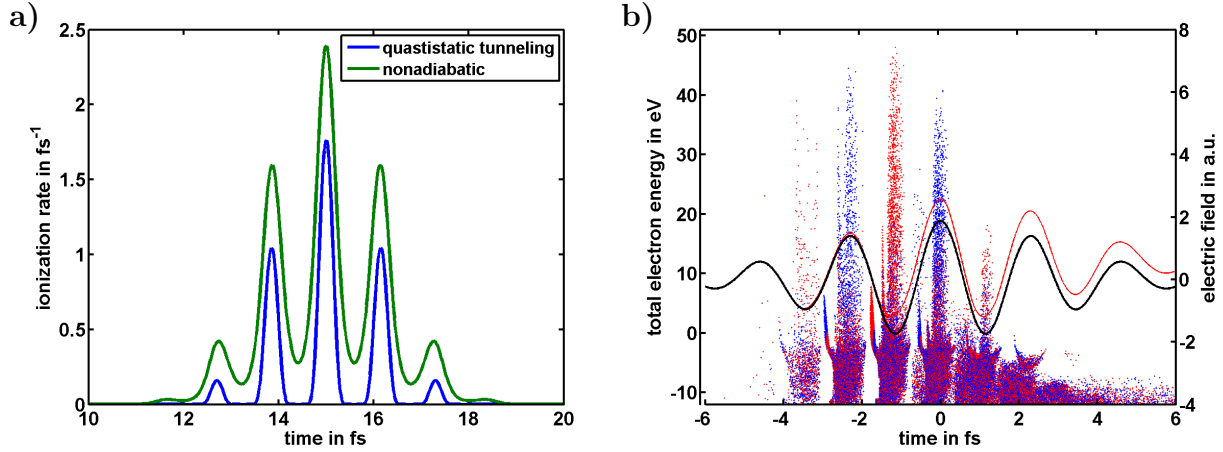


Figure 3.2: a) blue: quasistatic tunnel ionization rate in  $\text{fs}^{-1}$  during the laser pulse, green: modified non-adiabatic ionization rate, Keldysh parameter  $\gamma = 1.2$ ; b) same plot as in figure 3.1 but with a non-adiabatic ionization process instead of using the quasistatic limit, black: dielectric Mie-field at pole, red: total field including the meanfield

partially more favorable vector potential at birth time and therefore the electron can gain larger kinetic energies in the end. Moreover the non-adiabatic ionization process leads to an increased meanfield which directly results in higher kinetic energies of the direct electrons (almost 10 eV). On the other hand electrons born at the end of the laser pulse experience a stronger trapping potential which exceeds -10 eV in this case – compared to about -5 eV in the quasistatic regime. In general it can be said that the electrons occupy a larger volume in momentum space.

For very large Keldysh parameters  $\gamma \gg 1$  the modified tunneling model breaks down and also pure multi-photon-processes have to be considered.

### 3.3 Simulating attosecond streaking

To simulate attosecond streaking (see chapter 2.4) the code as outlined above is used for calculating electric fields from the IR-pulse and the electron propagation, but the photoemission of electrons by XUV-photons has to be included. Those electrons are referred to as XUV-electrons and are born all over the nanoparticle sphere with an emission depth of up to  $10 \text{ \AA}$  [27]. As shown later the inelastic mean free path has a larger influence on the streaking signal than the emission depth. XUV-electrons initially move radially away from the particle with a kinetic energy  $E_k = S_{\text{initial}} - I_p$  with  $S_{\text{initial}}$  being the Gaussian shaped spectrum (centered around 27 eV and  $2\sigma = 5 \text{ eV}$ , see figure 6.1a). After emission the electrons follow the total field, where they also experience the meanfield and scatter. The

XUV-electrons themselves do not generate a meanfield because their number is negligible compared to the number of IR-electrons. Elastic scattering uses the same energy-dependent mean free path as describes with formula 3.1 and acts isotropically. Impact ionization happens according to equation 3.2 and lowers the kinetic energy of the electron by  $I_p$  per inelastic scattering event. However in the implementation no new electron is generated since these electrons would not have enough energy to have any influence on the streaking trace in our region of interest. The different effects of inelastic and elastic scattering will be discussed in chapter 6.

The final electron spectrum is recorded in the direction of the IR polarization under a full opening angle of  $45^\circ$  to simulate the experimental setup.



# Chapter 4

## Experimental Setup

### 4.1 Generation of few-cycle laser pulses

The laser setup at the AS-5 beamline (Max-Planck-Institut für Quantenoptik, Garching) for the generation of few-cycle waveform controlled laser fields is based on a commercially available chirped pulse amplification (CPA) laser system (Femtopower Compact Pro). A Ti:Sapphire oscillator which is pumped by a solid-state laser produces a train of laser pulses of 6 fs pulse duration and a pulse energy of 3.5 nJ with a repetition rate of 70 MHz. Before amplification the pulses out of the oscillator pass through an acousto-optic programmable dispersive filter (Dazzler, Fastlite) to control the spectral phase and amplitude and are stretched by a SF-57 glass stretcher to a pulse duration of about 10 ps. These pulses are seeded into a ten-pass Ti:Sapphire amplifier where a fraction of them are amplified. The 2 mJ pulses at a repetition rate of 1000 Hz generated by the amplifier can be shared between the AS-5 beamline and the Petawatt Field Synthesizer (PFS) [28] with the help of a Pockels cell that turns the polarization axis at a rate of 500 Hz and a polarizing beam splitter.

The temporal compression of the pulse at the AS-5 beamline is achieved with a combination of a prism compressor in folded geometry and a number of chirped mirrors (16 times  $-500 \text{ fs}^2$ ). The fine adjustment of the dispersion is done by moving one of the prisms. To spectrally broaden the laser pulses the beam is then focused into a Ne-filled (typical pressure 3 bar) hollow core fiber (HCF) with a core diameter of  $275 \mu\text{m}$ . Because of the high intensities the Kerr effect leads to an intensity dependent refractive index which in turn changes the instantaneous phase of the pulse. This change leads to generation of new frequencies (Figure 4.2). Since those frequencies are not homogeneous in time (red-shifted part is generated in leading edge of pulse, blue on back side) another set of chirped mirrors (CM-58) is used to compress the broad spectrum after the fiber. To obtain the shortest

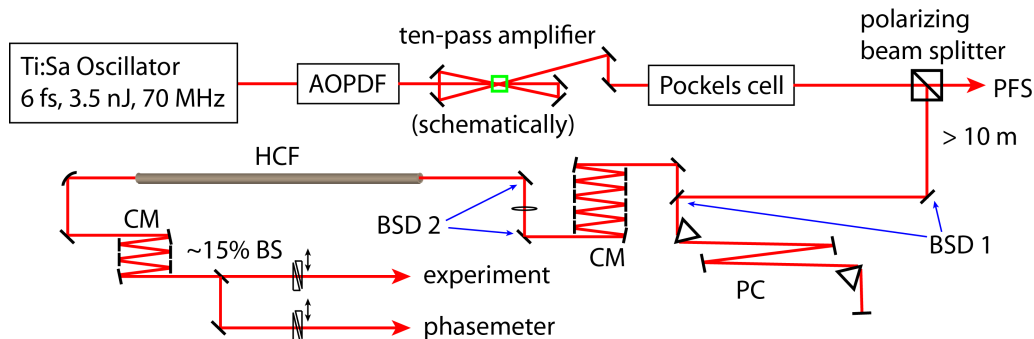


Figure 4.1: Setup of laser system. Description of all components can be found in the text. AOPDF: acousto-optic programmable dispersive filter, PFS: Petawatt Field Synthesizer, BSD: beam stabilization device, PC: prism compressor, CM: chirped mirrors, HCF: hollow core fiber, BS: beam splitter

pulse duration in the interaction region inside the experimental chamber a pair of movable fused silica wedges is used for fine control of the few cycle laser pulse dispersion. The Fourier-limit of the recorded spectrum would ideally allow a pulse duration below 3 fs (equation 2.2) but mirrors that do not support the full bandwidth of the spectrum and higher order dispersions lead to a slightly longer pulse. The possibility of CEP determination and especially High Harmonics Generation indicate that the pulse length is in the 5 fs regime.

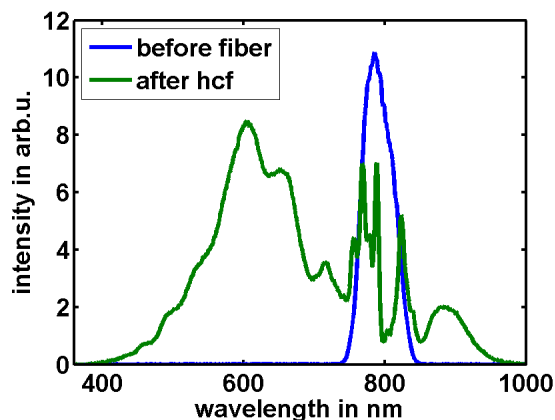


Figure 4.2: Blue: Laser spectrum measured before the beam enters the hollow core fiber, green: spectrum measured right after the fiber.

The quite long beam paths in the laser system (e.g. >10 m between the amplifier and the prism compressor) requires active beam stabilization in order to compensate mechanical instabilities and air fluctuations. At the AS-5 beamline two beam stabilization devices are used. Each stabilization system records the position and direction of the beam with a pair

of position sensitive detectors and controls two mirrors to keep both position and direction constant. One of those stabilizations is installed in front of the prism compressor and the other one stabilizes the beam going into the HCF.

## 4.2 Single-shot phase-tagged VMI

The single shot phase-tagged **velocitymap imaging** (VMI) setup consists of two main parts: The phasemeter and the experimental chamber with the VMI detector itself. The phasemeter is used to measure the CEP of every single pulse. This is done in a stereo time-of-flight chamber with a **microchannel plate** (MCP) on each side [29]. An MCP is an up to 1 mm thick plate made of highly insulating lead glass with metallic coating on both sides (electrodes) and is perforated by holes with a diameter of 25  $\mu\text{m}$  and a distance of about 30  $\mu\text{m}$  from each other. Single electrons that hit the MCP can be multiplied like in a photomultiplier tube when a high voltage is applied across the two electrodes. The current of those electrons can then be measured as a function of time-of-flight which can be used as a measure of the kinetic energy in the polarization direction. A gas cell inside the chamber is filled with xenon gas (ionization potential: 12.13 eV) and placed in the focus of the laser beam which interacts with the xenon and leads to photoemission of electrons that are detected by the two opposed MCPs. Two energy regions in the spectra are selected where rescattered electrons dominate. For both regions a so-called asymmetry parameter which is the signal difference between the two opposite directions normalized by the sum is determined. Both of those asymmetry parameters have a clear dependence on the CEP  $\phi_0$  that for some settings can have an offset of  $90^\circ$  for the high and low energy region [30].

Depending on the chosen energy regions the parametric plot of those two asymmetry parameters can give a more or less circular shape (figure 4.3). For each point, the angle  $\alpha$  relative to the center of mass of the plot can be calculated. Assuming a random CEP distribution for a typical period of time of a measurement the parametric angle  $\alpha$  can be mapped to the CEP  $\phi_0$ . There is still an arbitrary offset for  $\phi_0$  which is set to 0 because this technique can not measure the absolute CEP but only the relative CEP difference between the phasemeter and the experimental chamber.

The larger fraction ( $\sim 85\%$ ) of the beam is focused with a 50 cm focal length mirror into the experimental chamber. This vacuum chamber has a background pressure below  $5 \times 10^{-9}$  mbar when no gas load is applied. The laser focus lies between the repeller and extractor plates on the central axis of the VMI (see figure 4.4).

The VMI consists of three metallic plates to which different voltages are applied (repeller:  $V_{rep} = -15$  kV, extractor:  $V_{ex} = -12$  kV and ground: 0 V) and an MCP with a

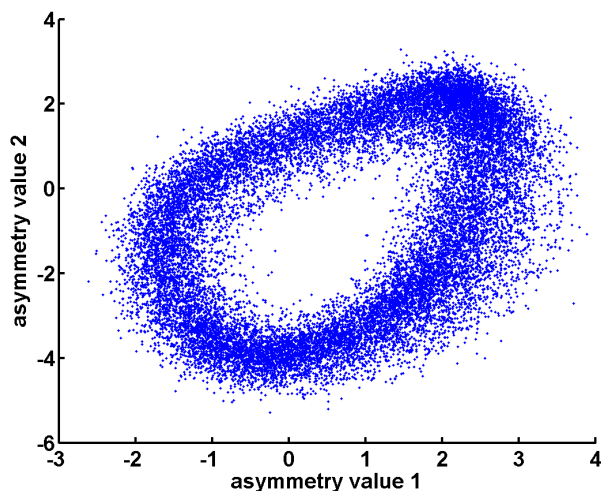


Figure 4.3: Parametric Asymmetry Plot for 20000 shots. Each point represents one laser shot recorded by the phasemeter. The two asymmetry parameters are calculated as described in the text and plotted with respect to each other. Out of this plot the parametric angle  $\alpha$  and the CEP  $\phi_0$  can be calculated.

phosphor screen. Those plates form a homogeneous static electric field in which electrons are accelerated towards the MCP. This whole section is shielded by a  $\mu$ -metal (not shown) to avoid any magnetic fields penetrating the chamber from outside. Simulations of electron trajectories show that for a certain ratio  $\frac{V_{ex}}{V_{rep}}$  all electrons with the same momentum component in the  $xz$ -plane hit the same position on the MCP, i.e. both the microscopic position differences at the beginning and the initial velocity in  $y$ -direction do not influence the detected position on the MCP. The absolute value of the voltages only shrink or magnify the image as long as the kinetic energy gained in the electric field is larger than the initial photoelectron energy. So with this setup it is possible to get the full 2D momentum projection of all electrons and in a system with a cylindrical symmetry with respect to the polarization axis  $z$  it is even possible to calculate the full 3D momentum distribution by an inverse Abel transformation.

In order to investigate isolated nanoparticles those particles have to be brought to the focal volume with a density that is large enough to have one interaction at least every 10–100 shots. The nanoparticles are suspended in solution (water or ethanol) with a concentration of 0.4–4 g/l and are sonicated shortly before use to break up possible cluster formations. The solution is dispersed in an atomizer ("Aerosol Generator 3076", TSI) which uses nitrogen as the carrier gas. The generated aerosol is further dried in a diffusion dryer filled with silica gel to remove the solvent. The following impactor is a sharp  $90^\circ$

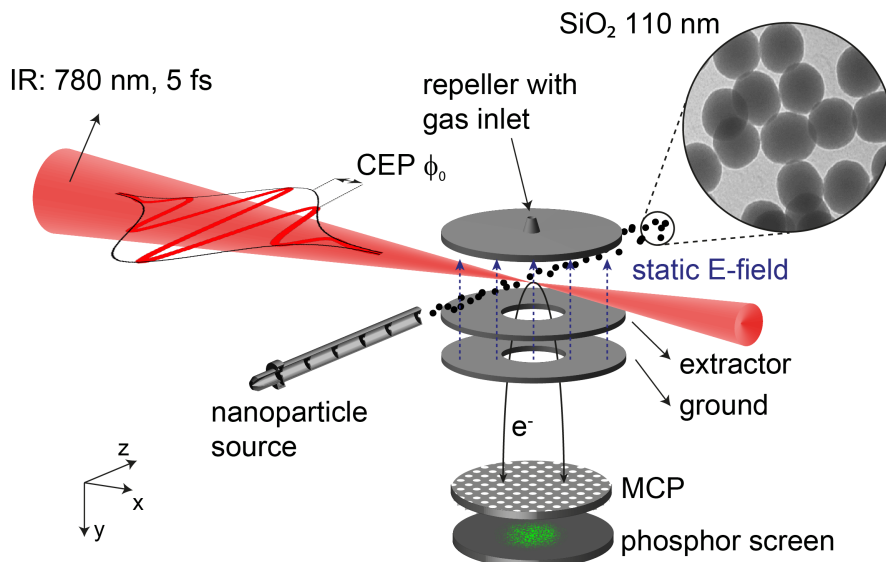


Figure 4.4: Sketch of VMI setup. In red on the left side: incoming few-cycle laser pulse with a certain CEP. From the front (in the polarization direction) nanoparticles are injected through an aerodynamic lens and intersect with the laser beam in its focus. This crossing lies between the repeller and extractor plate of the VMI. Photoionized electrons are accelerated in a homogeneous electric field through the holes in extractor and ground plate towards the MCP. They are multiplied there and made visible on the phosphor screen (not shown: camera which records images). Upper right: TEM image of monodisperse 110 nm diameter SiO<sub>2</sub> nanoparticles. For intensity calibration, the flow of particles is stopped and Xenon gas is injected through a small hole in the center of the repeller plate.

turn where single nanoparticles are light enough to follow the gas flow but much heavier clusters collide with the wall of this module and with high probability stick to the surface. An aerodynamic lens is used to bring all the particles to the center of the gas flow. This lens (diameter  $\sim 1.5$  cm) consists of several orifices with openings on the order of 1 mm at a distance from each other of about 5 cm. In "normal" laminar flow sufficiently small nanoparticles can follow the gas flow because of their small inertia and relatively large force exerted by the gas. In front of the entrance orifice the particles are brought to the axis of the aerodynamic lens but right behind the orifice the gas expands rapidly, leading to turbulent flow and leaving the particles close to the axis because of their inertia. How good this "centering" works depends on parameters such as the densities (of both gas and particle), pressure differences, diameters and the size of the particles. To make this lens work for a wide range of particle sizes orifices with different openings are used – each for a particular nanoparticle diameter. The last opening directly leads into the vacuum chamber and is about 12 cm away from the laser focus. Two differential pumping stages pump most

of the carrier gas before nanoparticles enter the VMI.

### 4.3 Interferometric attosecond streaking setup

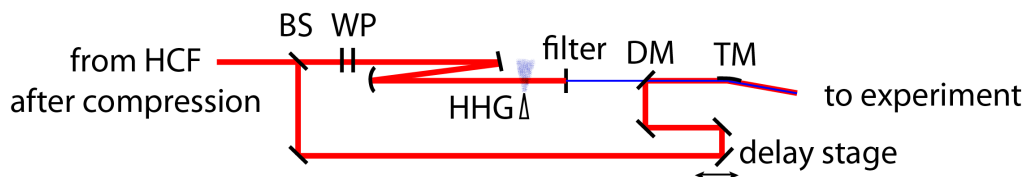


Figure 4.5: Setup of the streaking experiment. Description of all components can be found in the text. BS: beam splitter, WP: half-waveplate and quarter-waveplate, HHG: High-Harmonics Generation, filter:  $150\ \mu\text{m}$ -Al filter, DM: drilled mirror, TM: toroidal mirror.

The attosecond streaking experiments on isolated nanoparticles described in chapter 6 were done at the CUSBO laboratory at Politecnico di Milano. The laser setup for few-cycle laser pulse generation is similar to the laser system described in section 4.1 with the main difference that the amplifier generates CEP stabilized laser pulses with much higher pulse energy of 6 mJ. For efficient coupling of such intense laser pulses into the HCF a gas pressure gradient at the entrance of the fiber is realized by differential pumping. The spectrally broadened beam is split into two parts: one for XUV generation (pump) and one for the VIS/NIR probing pulse (figure 4.5). The probe is not modified and only travels through a delay stage to control the temporal delay between the two pulses. The high harmonics are generated with the help of the polarization gating technique [31]. This method uses a thick half-waveplate with the crystal axis set at  $45^\circ$  with respect to the laser pulse polarization axis. After the waveplate the two perpendicular polarizations have several fs delay. In regions with strongly different intensities (front and back of the pulse) this corresponds to almost linear polarization while the central part of the total pulse is circularly polarized. The subsequent quarter-waveplate changes the polarization pattern from linear-circular-linear to circular-linear-circular. Since the High Harmonic Generation (HHG) needs high intensities on the order of  $10^{14}\ \frac{\text{W}}{\text{cm}^2}$  the beam is focused right in front of a piezo-controlled valve and the phase-matching condition ensures that only the short trajectories are selected. The use of krypton as gas target for HHG leads to cutoff energies of about 37 eV (figure 6.1a). A  $150\ \mu\text{m}$  aluminium filter selects the high energy region above 20 eV and blocks the lower energies and the IR pulse. The XUV-pulse propagates through the central hole of a drilled mirror where it is combined with the IR-pulse from the other beam path. This interferometric layout allows for an adjustment of IR intensity

independent of XUV generation. A toroidal mirror ( $f = 80$  cm) focuses both beams at grazing incidence into the experimental chamber. The isolated nanoparticle beam was delivered to the interaction region similar to the process described in section 4.2. For photoelectron detection in the direction of the laser polarization a TOF spectrometer was used. The transmitted laser beam is sent into a grating spectrometer combined with an MCP to monitor the XUV spectrum during the measurement.

A 100 as temporal delay between the pump and probe arms of the interferometer corresponds to a relative change in the beam path of only 15 nm. Since on this length scale vibrations, changes of the refractive index in air, and thermal expansion of mirrors and mirror holders become relevant, a system for stabilization of both arms of the interferometer was installed. A HeNe-laser (632 nm) is coupled in before the beamsplitter separating VIS/IR- and XUV-paths and coupled out before the recombination mirror thus experiencing the same changes in travel distance as the two experimental beams. The two parts of the beam from both arms are overlapped on a camera after using a chopper to block the (more intensive) VIS/IR-pulses. The phase of the interference fringes now show the changes in path length in the two different arms. This can be used to stabilize the setup and keep the relative delay between pump and probe constant.

## 4.4 Sample preparation

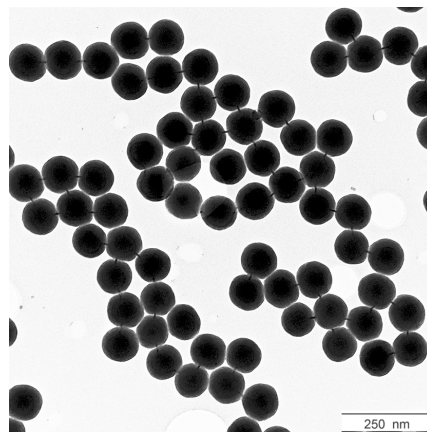


Figure 4.6: TEM image of 100 nm polystyrene particles. The image shows a monodispers polystyrene solution. The lines between the particles are an artifact of the measurement technique for organic materials. In solutions no evidence for cluster formation was found. By courtesy of Christian Schäfer.

The 100 nm SiO<sub>2</sub> and polystyrene nanoparticles are prepared by the Stöber method [32].

This method uses a small seeding particle and grows by accretion of monomers or oligomers, respectively – resulting in a particle with an onion-like structure (figure 4.6). The 110 nm ZnS particles are grown from many small nanoparticles that aggregate and finally form a larger one. This mechanism is similar to the Ostwald ripening of liquid sols. When using the right parameters such as concentrations and temperatures the resulting solution can be made very monodispers with a standard deviation of  $\sim 5\%$ . The samples have been prepared in the groups of Prof. Eckart Rühl and Prof. Christina Graf (FU Berlin, SiO<sub>2</sub> particles), Prof. Matthias Rehahn, Dr. Markus Gallei and Christian Schäfer (TU Darmstadt SiO<sub>2</sub>, ZnS and polystyrene particles) and Prof. Jinwoo Lee and Minsu Kim (POSTECH, Korea, 100 nm Fe<sub>3</sub>O<sub>4</sub> particles).

# Chapter 5

## Photoemission from nanoparticles in strong IR-fields

To understand the photoemission process from nanoparticles in detail it is important to know the exact effect of a given electric field on the particle and all ionized electrons. The setup described in chapter 4 on the one hand enables to retrieve the waveform of the electric field interacting with the particle by means of the phasemeter and on the other hand gives information about the final velocities of all electrons with the help of the VMI. We want to draw conclusions from the final distribution of those electrons and out of that gain insight into the microscopic movements and interactions that play an important role in strong field photoemission.

The combination of those two important components allows to gain deeper insight in the photoemission process. After the description of all methods and required calibrations the analysis is exemplified on  $\text{SiO}_2$  nanoparticles including comparison with simulations. This already shows the most important aspects of the ionization process and electron propagation. A study of different substances points out the influence of certain material properties on those effects and permits to draw conclusions on our numerical model.

### 5.1 Methods

For a comparison of the obtained measurements with theory and simulations accurate knowledge of the laser intensity is important in order to understand the nonlinear processes taking place. Calculating the intensities out of measured beam parameters (which are partly hard to determine exactly) would induce large errors. To circumvent this limitation intensity calibration scans in xenon gas are performed and the photoelectron spectra are recorded. For these experiments the nanoparticle source is shut off and xenon gas is fed

through the repeller into the chamber.

Light signals on the phosphor screen of the VMI are recorded by a fast camera so the total projected two-dimensional electron distribution can be captured. The whole setup works in single-shot mode and as a result the assignment of CE-phase information to each electron image is well-defined. Since it is not possible to record an image with  $1280 \times 1024$  pixels<sup>2</sup> every 1 ms a threshold system for the reduction of information is necessary. Every pixel with an intensity below a certain threshold is neglected. This way the momenta of up to 1024 electron hits per laser shot can be stored. During post-processing the phases are distributed over 20 bins and each shot is assigned to one of them. Details are described in [33].

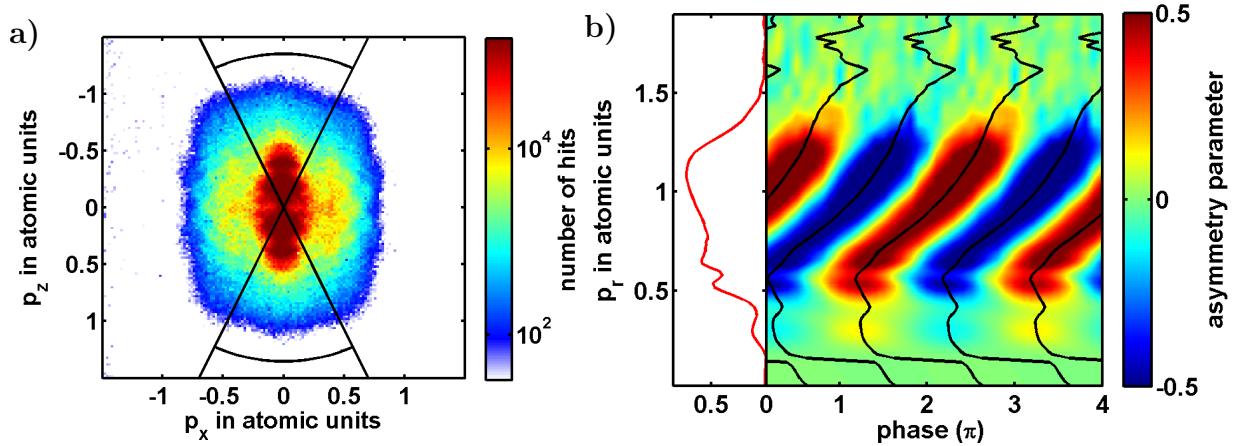


Figure 5.1: a) Momentum plot of an intensity calibration scan with xenon gas. This plot shows the electron distribution of a xenon measurement with an intensity  $I = 5.3 \times 10^{13} \frac{\text{W}}{\text{cm}^2}$  on a logarithmic scale. Close to the center two ATI-peaks can be seen in both positive and negative  $z$ -direction. The black lines show the two angles used for asymmetry calculation. b) Corresponding relative asymmetry plot. In the lower momentum part the asymmetry parameter is low due to contributions of electrons with different phase dependencies. Above that region the asymmetry is increasing up to the cutoff of almost 1.5 a.u.. This region shows a phase shift of almost  $2\pi$  across the entire momentum region. Above this part noise gives a random phase behavior. Red line on the left: Amplitude of asymmetry oscillation for each momentum  $p_r$ .

To get a first impression of the electron distribution all frames are summed up and shown in a momentum plot (figure 5.1a). Because of the high count rate the total dynamic range is quite large and a good signal to noise ratio is achieved. In the low energy region at least two distinctive ATI-peaks can be seen in both up and down direction which are separated by one photon energy. The plot shows all expected asymmetries along the  $x$ - and  $z$ -axes but a slightly higher efficiency of the MCP on the right side is visible.

To retrieve the phase dependence the CEP-binned images are evaluated individually. For each phase bin two sectors with  $50^\circ$  full opening angle are chosen in the polarization direction (black sectors): one pointing upwards, the other one pointing downwards. Out of those two signals ( $S_{up}$  and  $S_{down}$ ) a relative asymmetry parameter  $A = \frac{S_{up} - S_{down}}{S_{up} + S_{down}}$  is determined which is dependent on the radius. This parameter – equivalent to the definition in chapter 4 for the phasemeter – expresses the difference of electron emission for two opposite directions. In figure 5.1b the parameter  $A$  is plotted for all phases and radii. The asymmetry can be assumed as a harmonic function of the CE-phase with its strength and shift depending on momentum/energy [34] (without higher harmonics:  $A(\phi_0, p_r) = S(p_r) \cos(\phi_0 + P(p_r))$ ). The "shifting" is indicated by the solid black lines (phase  $P(p_r)$ ) and the asymmetry strength can be read off on the left (strength  $S(p_r)$ ): The red line is showing the amplitude of the asymmetry.

Above a plateau of almost constant count rate the spectrum shows a drop in count rate which we define here as the cutoff. This can easily be seen in the asymmetry plot. For electron counts being lower than the noise of the MCP the phase dependent asymmetry can not be resolved anymore which reveals itself as a falling asymmetry amplitude and a fluctuating shift above  $\sim 1.5$  a.u. in figure 5.1b. On the left side the red curve shows the asymmetry amplitude which is used to determine the cutoff and to calculate the laser intensity. The cutoff energy  $E_{\text{cutoff}} = \frac{p_{r,\text{cutoff}}^2}{2 \cdot m}$  is defined as the energy for which the asymmetry parameter is equal to the noise level. In case of xenon the asymmetry parameter is well above 0.5 and indicates a clear cutoff at  $\sim 1.5$  a.u.. The shift in the carrier-envelope phase dependence (solid black line) is quite large and explains why the technique used in the phasemeters works so well with xenon gas: It is easily possible to find two momentum regions that show a shift with a difference of  $\sim \pi/2$  and also have a large enough signal.

The strong-field ionization process from single atoms (like in the case of the noble gas xenon) is much better understood than for solids. From the known ionization potential  $I_p = 12.13$  eV of xenon the intensity can be calculated by the evaluation of the cutoff (see cutoff law, equation 2.9). For each nanoparticle scan the laser beam is attenuated by a circular continuous neutral density filter and measured with a powermeter to calculate the intensity from the xenon calibration. This method was tested for several cases and proved to work under all tested conditions: Different filter positions (i.e. different pulse energies) and also several voltage settings of the VMI lead to a changing image size of the momentum distribution. The use of NO gas (nitric oxide) in addition to Xenon makes it possible to extend the method to even lower intensities due to the low ionization potential ( $I_p = 9.26$  eV). The retrieved calibration agrees well with the xenon data (figure 5.2a).

Similar to the calibration of intensity (retrieved from a pulse energy measurement) a

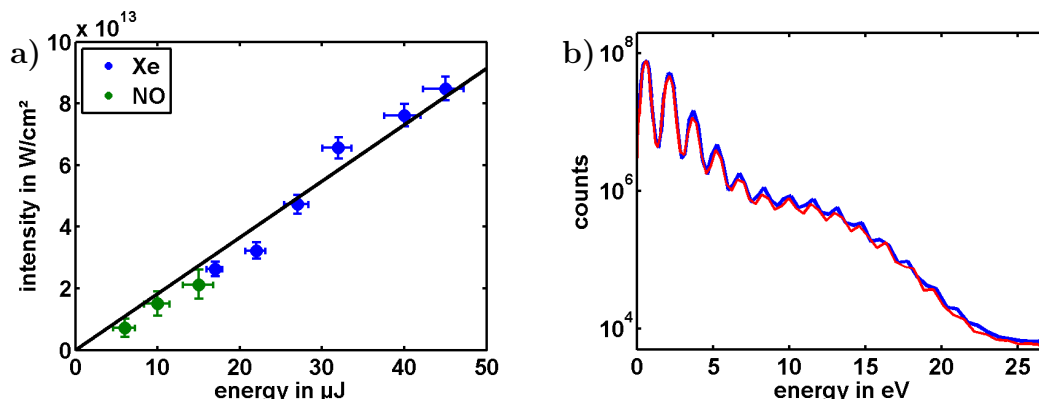


Figure 5.2: a) Calibration of intensity. Several measurements were taken in different gases (NO and xenon) at different background pressures. The pulse energy was varied by a neutral density filter. The intensity was calculated using the cutoff in the asymmetry plots and equations 2.9 and 2.7. The plotted points show the expected proportional dependence between energy and intensity and the fitted line (black) is further used for calibrating the nanoparticle scans. The two measurements in xenon with the highest energies used higher extractor and repeller voltages. b) Photoelectron spectrum from xenon gas with long laser pulses with a narrow spectrum. The laser pulse out of the compressor is – without passing the HCF – sent directly into the experimental chamber. The blue and red lines show the number of counts in up and down direction, respectively, on a logarithmic scale. The abscissa is converted from pixels to energy. The spectrum shows ATI-peaks separated by one photon energy which allows the calibration of energy.

calibration of the MCP detector has to be done. How much momentum corresponds to a pixel on the camera? Again, in principle this could be done by trajectory calculations of electrons in electric fields but the exact geometric dimensions of the VMI setup have to be known. An easier way is to use a feature that has already been mentioned in figure 5.1a: ATI-peaks. For the energy calibration the hollow core fiber is bypassed and thus longer pulses with a much narrower spectrum are generated. When using this laser pulse the generated electron spectra show many, clearly distinct ATI peaks all separated by one photon energy (figure 5.2b). This measurement gives the information to calculate the momenta (and energies) out of pixel positions.

## 5.2 Experimental results from SiO<sub>2</sub> nanoparticles

Nanoparticle measurements are performed with the methods described in chapter 4. The obtained electron distributions are treated similar to the xenon case just with smaller variations. First, in a nanoparticle measurement most of the recorded frames actually contain

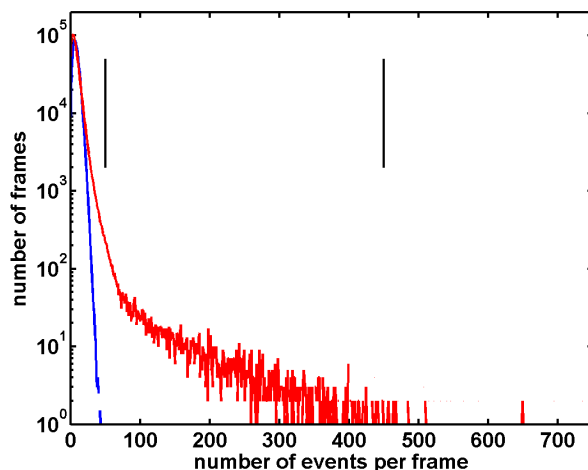


Figure 5.3: Histogram showing number of events per frame for nanoparticle scan (red) and reference scan in ethanol (blue). In both scans most frames are in region on the left with no or only a few events per frame (up to  $\sim 50$  events). The central part of the nanoparticle histogram belongs to events from nanoparticles (50–450 events). Above 450 events almost no signal from clusters can be seen. The threshold value in the acquisition software shifts this histogram: The optimal setting ensures that almost all frames contain less than 1024 events and the count rate from nanoparticles is still high enough allowing the separation from noise and gas contribution.

only electrons emitted from gas atoms or molecules so a larger number of laser shots is necessary to achieve a comparable statistics. Second, those frames with undesirable events have to be sorted out for further analysis but can we distinguish gas from nanoparticle hits?

The number of hits in each single image is used for this decision. The distribution of those numbers is shown in figure 5.3 as a histogram (nanoparticle scan in red). All frames with a low number of hits can be assigned to either just noise from the MCP/phosphor screen detector and CMOS-chip or a signal from background gas (blue) in the vacuum chamber. Those frames are much more frequent than nanoparticle hits (note the log-scale). Nanoparticles lead to both higher energy electrons ( $>50$ ) and larger number of electrons which can be seen in the measurement and used for separating them from background gas. In addition to that nanoparticles can aggregate and form clusters composed of several single particles. If those are hit by the laser pulse and ionized even more electrons will be emitted – in the software 1024 hits are detected. Figure 5.3 does not contain many frames with clusters but for example the frames with 650 hits will be neglected in order to suppress any signal from clusters. Altogether the histogram can be used to extract

the nanoparticle frames while neglecting noise from unwanted events. In the histogram in figure 5.3 the nanoparticles are in the region between 50 and 450 events per frame.

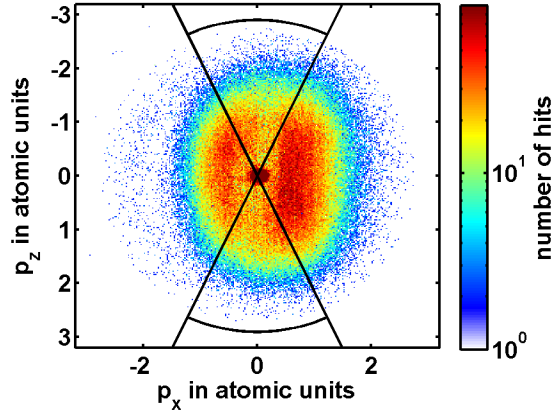


Figure 5.4: Momentum plot of 80 nm SiO<sub>2</sub> particles. This plot is showing the electron distribution of a SiO<sub>2</sub> measurement with an intensity  $I = 4.2 \times 10^{13} \frac{\text{W}}{\text{cm}^2}$  on a logarithmic scale. The center with zero momentum is clearly visible. In direction of the polarization (up/down,  $z$ -axis) the spectrum almost reaches the edge of the circular MCP detector which is at  $\sim 2.8$  a.u. In the propagation direction (from left to right,  $x$ -axis) the absolute value of momenta is lower. Asymmetries in this direction are mainly caused by inhomogeneities in the MCP efficiency. This also is true for the reduced count rate directly along the  $z$ -axis. The black lines show the two angles used for asymmetry calculation.

All the frames from that region are summed up to give a first impression of the electron distribution like in the case of xenon. Figure 5.4 shows this distribution in a logarithmic false color plot for a measurement of 80 nm SiO<sub>2</sub> nanoparticles at a peak intensity  $I = 4.2 \times 10^{13} \frac{\text{W}}{\text{cm}^2}$ . Not all nanoparticles however experienced this peak intensity because in the experiment all scans are intrinsically focus/volume averaged. This means that electrons (except in the cutoff) can either belong to the group of low energy electrons from nanoparticles hit in the center of the laser focus with a high intensity or belong to the group of high energy electrons from nanoparticles that experienced only a lower intensity out of the focus.

The particles have been dissolved in ethanol and nitrogen was used as a carrier gas. For this run 1.6 million shots have been recorded but only a fraction contains nanoparticles and is used for further investigation. The polarization axis of the incoming laser beam is in the plane of the detector in  $z$ -direction. On this axis the field enhancement leads to the highest final energies which can already be seen in this plot. The cutoff is  $\sim 2.6$  a.u. and already close to the edge of the detector at  $\sim 2.8$  a.u. The laser beam propagation is from left to right in  $x$ -direction. Asymmetry in this direction mainly comes from inhomogeneities in

the MCP efficiency. This effect can also be seen directly on the  $z$ -axis where the signal is slightly bleached out.

The described symmetric elliptical shape is typical for small particles ( $d \ll \lambda$ ) that have a mostly dipolar-like response to the few-cycle-laser pulse. The up-/down-symmetry however is broken if one looks at the CEP-dependent signal instead of the averaged momentum plot.

With the same procedure as described in section 5.1, an asymmetry parameter is calculated for SiO<sub>2</sub> nanoparticles and shown in figure 5.5. At low momenta the signal is a mixture of background gas and nanoparticles. Because of volume averaging the resulting asymmetry parameter gets washed out in that energy region. On the contrary the region of high momenta electrons is much more selective.

Rescattered electrons from xenon atoms can gain a maximum momentum of 1.36 a.u. according to equation 2.9 so all signal above that limit has to originate from nanoparticles near the center of the laser beam. Because high electric fields are required the electrons in the cutoff region probe the regions with the highest field enhancements, which are the fields around the poles in the polarization direction.

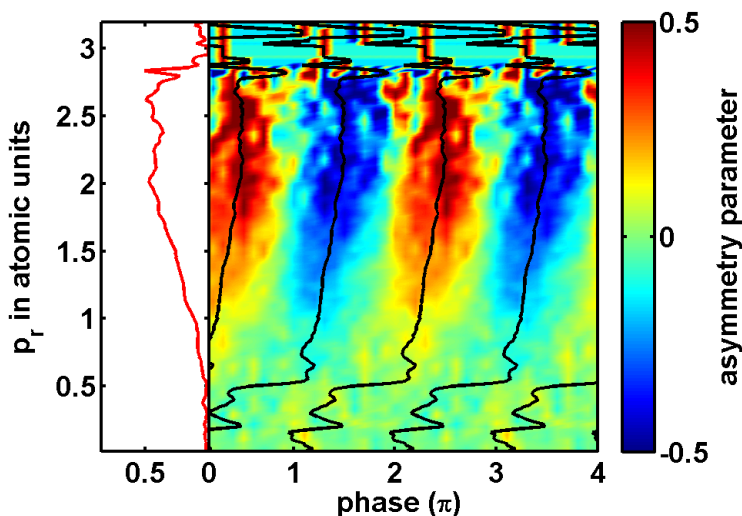


Figure 5.5: Asymmetry plot for 80 nm SiO<sub>2</sub> particles,  $I = 4.2 \times 10^{13} \frac{\text{W}}{\text{cm}^2}$ , in false colors. Obtained from the data shown in figure 5.4. For this asymmetry plot two sections with an opening angle of  $50^\circ$  are selected in the polarization direction in the momentum plot. The momentum dependent asymmetry parameter is calculated as described in the text and further plotted for each phase bin which is measured by the phasemeter. The solid black lines show the shift of the asymmetry value  $P$ . The red line shows the asymmetry amplitude  $S$ . The MCP detector ends at  $\sim 2.8$  a.u.

The shape of this asymmetry map can be used for a first evaluation of the measurement

to estimate the contribution of background gas to the nanoparticle signal. The asymmetry amplitude gives information about the pulse length since only few-cycle pulses lead to a strong CEP dependence. The shift of the asymmetry with CE-phase  $P(p_r)$  is indicated again by the black line and is not as pronounced as for xenon. The cutoff value can be read off from the red line indicating  $S(p_r)$ . It is not influenced by the type of carrier gas which only affects lower energies and is quite sensitive to the field enhancement around the poles for example. This property enables the comparison with simulations and the extraction of electric field distributions around the particle as well as material properties like scattering or ionization probabilities.

A complete understanding of the ionization and propagation processes can be obtained by inspecting the complete 2D asymmetry map instead of only the one in polarization direction. For each pixel the phase dependent signal is Fourier transformed in order to obtain information about the asymmetry for each point in momentum space. The amplitude and phase of the first Fourier component can be seen in figure 5.6.

Figure 5.6a shows the logarithmic (absolute) asymmetry amplitude of each pixel, i.e.  $p_x$ - $p_z$ -momentum component. While in the propagation direction the asymmetry is much weaker the strongest contribution is given by electrons of the plateau region that form two separated half circles in this plot ( $p_z = \pm 1-2$  a.u.).

The phase of the first Fourier-component is plotted accordingly on a color scale from 0 to  $2\pi$  (figure 5.6b). For very high momenta where only noise is detected phases are random and don't have any physical meaning because of the infinitely small amplitude in the asymmetry signal (see figure 5.4 or also the region above the cutoff in figure 5.5). Therefore the phase map is overlaid with the logarithm of the signal as a transparency function leading to a fading out in the noise region. The tilt of the solid black line in figure 5.5 is also apparent in the phase map. Following radial lines beginning in the center of the map a shift in phase can be recognized as a color shift from blue to red or vice versa. For gases this shift is much stronger and influences the central, low momenta region. For higher energies where nanoparticles make the largest contribution this shift gets weaker and finally reaches a constant shift in the cutoff region. It is clear that the upper and lower half are almost perfectly phase-shifted by  $\pi$ . From this plot the exact response of electrons on a certain shape of the electric field can be extracted. Only for certain shapes the highest acceleration of electrons is achieved and those electrons can show up as cutoff electrons. This selectivity allows to gain insight into the interaction mechanism between the nanoparticle, the dielectric field, the meanfield and the electrons. Herewith also ionization and scattering processes can be further investigated.

Figure 5.6c shows the same information as the amplitude plot in figure 5.6a and helps

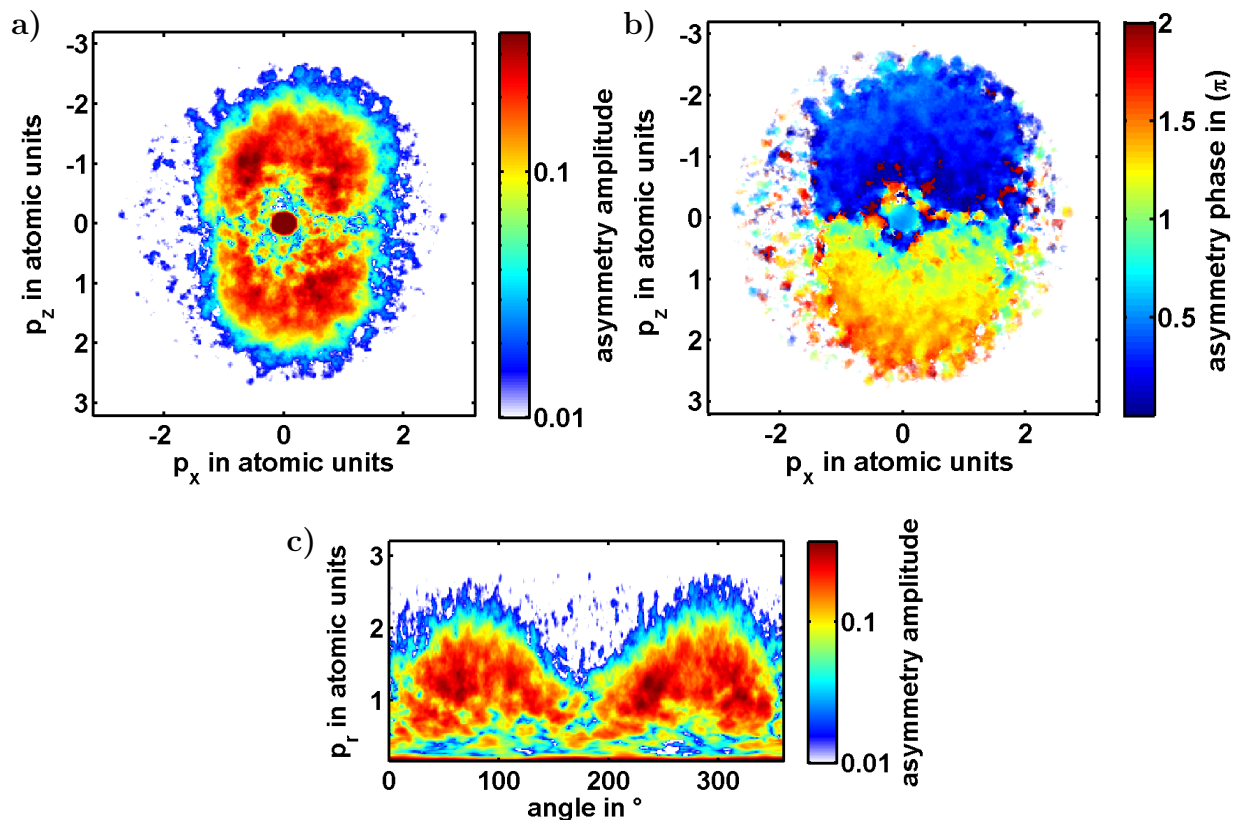


Figure 5.6: Asymmetry map of 80 nm SiO<sub>2</sub> particle, same measurement as before. a) Asymmetry amplitude: The Fourier-transform of the CEP-dependent signal is calculated for each pixel giving a map of asymmetry values for all momenta. b) Retrieved phase of the asymmetry oscillation with CEP, obtained from the Fourier analysis. c) Asymmetry amplitude in polar coordinates: angle measured from the backside of the particle and radial momentum.

to understand the angular dependencies of electron emission in strong fields. The axes are converted to polar coordinates (angle relative to positive  $x$ -axis). This shows even more clearly that the electrons with the highest momenta originate from the regions around the poles (in polarization direction) where the highest field enhancements occur. The small deviation between the angle of maximum cutoff momentum and  $90^\circ/270^\circ$  is mainly due to the fact that the MCP has a region on the left side with lower detection efficiency.

The analysis of both SiO<sub>2</sub> and xenon measurements reveal the most important mechanisms that drive the photoemission in strong fields. The distribution in momentum space is recorded by VMI-images and the cutoff energy gives information about the accelerations and field strengths occurring around nanoparticles. Taking into account the strongly CE-phase dependent signal it is obvious that changes of the electric field in the sub-cycle regime

play an important role for the ionization and electron dynamics. For a full understanding of those processes taking place on an attosecond timescale an even closer look is necessary. With the help of simulations it is possible to investigate the influence of different effects like the ionization itself, electron scattering in the nanoparticle, electric field distributions around dielectrics and the interaction between charged particles.

### 5.3 Simulations

To simulate the described experiments the M<sup>3</sup>C-Code as described in chapter 3 was used. The simulations were performed with the same laser parameters as the experiment. The laser has a central wavelength of 700 nm and a pulse duration of 5 fs. In all simulations dielectric fields are calculated with the material specific permittivity, density and ionization energy while meanfield effects contribute to the total field.

First, simulations were carried out and compared with the experimental results. A comparison can give information about important effects for photoemission in strong fields and answer the question if the theory describes all physical processes sufficiently correct. Deviations between the experiment and simulations demand for a closer look at certain aspects and might help to understand so-far neglected effects.

Second, in simulations it is possible to access information which is almost impossible to obtain from the experiment. For example electrons can be sorted by the number of performed collisions or birth positions to get a deeper understanding of the effect of rescattering or near fields close to the particle surface. Other aspects are the dependence of the electron birth time on the ionization mechanism or the influence of the meanfield on the electron trajectories. Those results can partly be retrieved from experimental studies (see also chapter 6) but are directly accessible in simulations.

In the following plots the same methods were used as described in chapter 5.2. Simulations are done at  $I = 4.0 \times 10^{13} \frac{\text{W}}{\text{cm}^2}$  with 100 nm SiO<sub>2</sub> nanoparticles using the dipole approximation. In figure 5.7a all electrons are shown that have positive total energy to overcome any trapping potential and are outside the particle. The focus averaging<sup>1</sup> in-

<sup>1</sup>Focus averaging of the signal  $S(I)$  is done in the plane perpendicular to the propagation with an assumed intensity  $I(r) = I_0 \exp\left(-\frac{r^2}{w_0^2}\right)$ . The averaging itself is done by

$$\int \int S \cdot r \, d\varphi \, dr = 2\pi \int S \frac{dI}{-\frac{2}{w_0^2} I_0 \exp\left(-\frac{r^2}{w_0^2}\right)} = -\frac{w_0^2}{2} 2\pi \int S \frac{dI}{I}.$$

So in the discrete case a series of scans with equidistant intensities is weighted with  $I^{-1}$  and summed up.

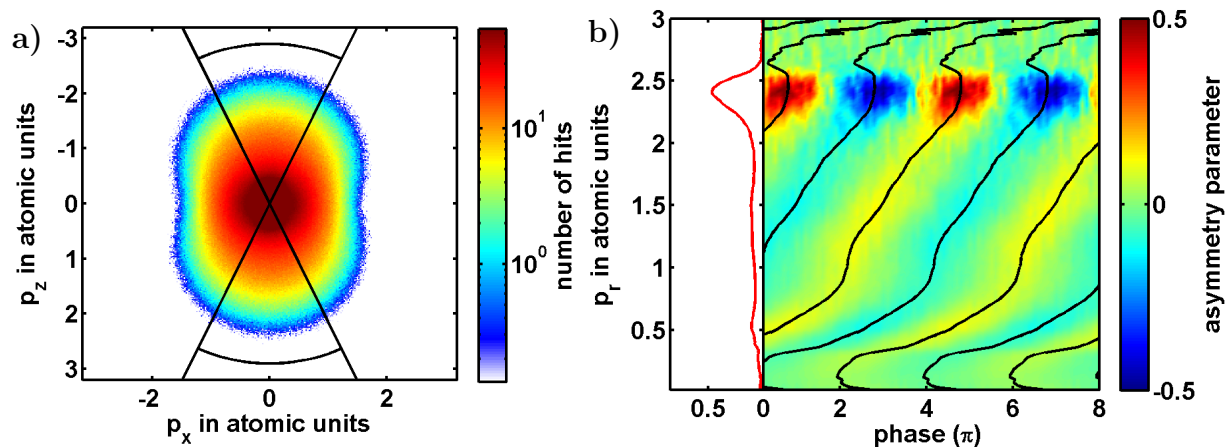


Figure 5.7: a) Momentum plot for simulated  $\text{SiO}_2$  nanoparticle in 5 fs laser pulse with  $I = 4.0 \times 10^{13} \frac{\text{W}}{\text{cm}^2}$  (focus averaged). This plot shows the projected electron distribution on a logarithmic scale. The black lines show the two angles used for asymmetry calculation. b) Corresponding relative asymmetry plot. In the lower momentum part only a low asymmetry can be seen due to lack of background gas and high contributions from electrons with high numbers of scattering events. High asymmetry only occurs in the region of the cutoff because in simulations only few specific CE-phases lead to high energy electrons. Some artificial noise was added in order to see the transition from the cutoff region to regions without signal.

cludes scans with a step size of  $0.5 \times 10^{13} \frac{\text{W}}{\text{cm}^2}$ . The final momenta are projected onto the detector plane and shown in a logarithmic plot. This plot confirms the observed behavior of electrons which gain the highest energies in polarization direction. The highest field enhancements occur at the poles and finally are responsible for the lobes in  $z$ -direction.

In simulations the cutoff depends on the statistics due to the exponential decrease in signal for high momenta. Therefore in the calculation of the asymmetry plot (figure 5.7b) some artificial noise was added in order to obtain the same dynamical range as in the experiment. By determining the cutoffs in simulations as the point where the asymmetry meets the level of noise an influence of overall statistics can be excluded. The different shape of the asymmetry plot is due to the fact that contributions from the background gas are not included. So the low energy region is dominated by electrons with a high number of collision. They have no specific phase dependence and lower the relative asymmetry. Nevertheless the cutoff energy retrieved from the simulation is not affected by this effect and agrees well with the experimental data (see measurement in figure 5.5).

Complete asymmetry maps reveal the same cutoffs and phase dependencies (figure 5.8) as the experiment. The absolute asymmetry map reflects the momentum map with a similar shape and the two cutoff regions form semicircles. Those semicircles can also be

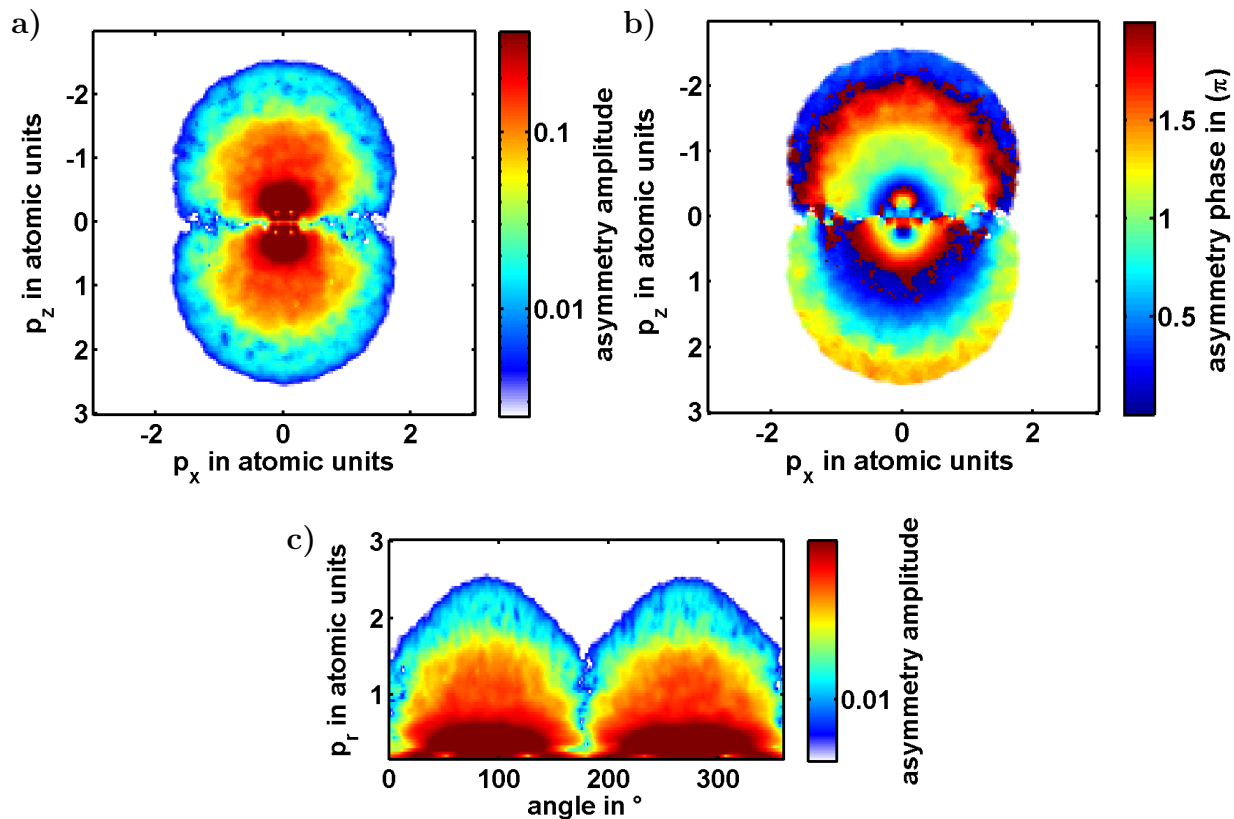


Figure 5.8: Asymmetry maps from simulations of SiO<sub>2</sub> nanoparticles. a) Asymmetry amplitude. Covers a similar shape as the momentum map. Two separated half rings can be seen in the cutoff region that correspond to the high relative asymmetry in figure 5.7b. b) Asymmetry phase plot shows shift of almost  $2\pi$  and equal behavior in upper and lower half circle. c) Asymmetry amplitude in polar coordinates. Shows same data as figure a) but for radial and angular component. Highest cutoff is reached in up- and down-direction at  $90^\circ$  and  $270^\circ$ , respectively.

identified in the asymmetry phase plot. From the cutoff region to the center of figure 5.8b a continuous transition of colors traces the shift that is also seen in figure 5.7b.

## 5.4 Comparison between experiment and simulation

The Simulations show a good agreement with the experimental results. Although at low momenta the experimental data is superimposed with a signal from background gas the main characteristics in momentum and asymmetry plots can be reproduced. At high momenta the simulations provide excellent predictions of the measured cutoff. This parameter will be used for further investigation of material properties and the response of

the nanoparticle to the laser pulse.

To validate the theoretical considerations used in the simulation model both experiments and simulations were performed for different conditions. First the intensity dependence of the cutoff is investigated. For the range of  $1\text{--}5 \times 10^{13} \frac{\text{W}}{\text{cm}^2}$  the maximum final energy achieved by electrons from SiO<sub>2</sub> nanoparticles is found to scale linear with intensity with a factor of approximately

$$E_c = 50 U_p \quad (5.1)$$

thus staying constant when measured in terms of  $U_p$  instead of eV (referred to as the *relative* cutoff). This value also agrees well with earlier measurements done on SiO<sub>2</sub> nanoparticles [11].

Direct electrons from *atoms* are expected to gain  $2U_p$  in linear polarized laser fields while rescattered electrons achieve  $10U_p$  [35] following the classical cutoff law. More than ten years after the publication of the classical law a quantum-mechanical modification was presented [18]. This law was used in the xenon measurements for intensity calibration (equation 2.9). In contrast to gases, photoemission from nanoparticles leads to much higher electron energies which will be explained in the next paragraphs.

The electron emission and acceleration from nanoparticles is quite different from that in atoms or molecules. A rather obvious difference lies in the fact that the dielectric nature of SiO<sub>2</sub> leads to a field enhancement around the particle of a factor of  $\alpha = \frac{3\epsilon}{2+\epsilon}$  for small particles. Since all electrons remain close to the particle during the laser pulse they experience the increased near-field and a modified ponderomotive potential  $U_p^* = \alpha^2 U_p$ . In the case of silica the expected classical cutoff would be around  $E_c \approx 10 U_p^* = 23.8 U_p$  accounting for the field enhancement and rescattering. A closer look on the simulated field evolutions will help to understand why the observed cutoff is more than two times higher than expected. Not only the laser field influences the ionization process and electron dynamics but also the interaction between the electrons themselves has a large impact. Figure 3.2b shows the total field at one pole during the laser pulse compared to the Mie-field. Once the first electrons are ionized they start to form a meanfield that influences other electron trajectories but also the ionization probabilities for future time steps. During one half-cycle this can be interpreted as some saturation effect because ionization will take place until the Coulomb repulsion of a sufficient number of electrons counteract the laser field and no further ionization takes place. The total number of electrons is – in first order – determined by the field strength and not the ionization rate, yet changes in birth position or time might have a considerable influence on final energies.

The larger absolute fields resulting from meanfield effects lead to the measured cutoffs

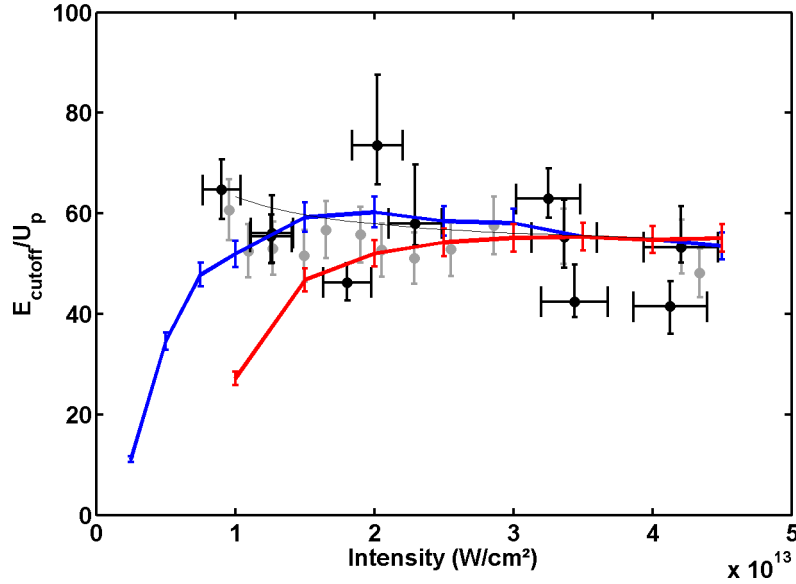


Figure 5.9: Measured and simulated cutoff energies of  $\text{SiO}_2$  nanoparticles for different intensities. The intensity denotes the peak intensity retrieved from reference scans in xenon gas as described in section 5.1. The cutoff is displayed in units of  $U_p$  which is proportional to the intensity  $I$ . Black points refer to experiments done in the scope of this thesis and grey ones belong to earlier measurements [11]. The lowest intensity is determined by the signal to noise ratio at small laser pulse energies and the highest intensity is limited by the voltage of the repeller plate and the size of the MCP. The red line shows the cutoff which is obtained from simulations using the quasistatic ionization model and the blue line corresponds to simulations with the exact same parameters except using the non-adiabatic ionization model. Both simulations use the bulk work function for  $\text{SiO}_2$  of  $I_p = 9.0$  eV and permittivity of  $\epsilon_r = 2.12$ . The thin line illustrates the cutoff law from equation 5.2.

of about  $50 U_p$ . This is confirmed for most of the measured and simulated intensities except for the very low intensity range. The simulations including the quasistatic tunneling model reveal a decreasing *relative* cutoff for intensities below  $2.0 \times 10^{13} \frac{\text{W}}{\text{cm}^2}$  which is not consistent with the measured values. In principle several factors could be responsible for this discrepancy. First of all the intensities in the experiments have to be precisely determined because of the direct influence on the intensity scale but also the indirect effect on the cutoff through  $U_p$ . This is assured as described in section 5.1 and can not be responsible for such large deviations. Second systematic errors in the setup have to be excluded, e.g. errors due to the detection setup, different particles or laser parameters than assumed. All those possibilities have been checked during several measurements under different conditions and still the same trend was observed. The relative cutoff for low intensities is not decreasing but staying constant or even rising above  $50 U_p$ . The third

possibility is an effect that occurs during experiment but is not considered in the simulation model.

For very low intensities the Keldysh parameter gets larger than 1 which means that the treatment of the ionization process as pure tunneling is not valid anymore. As described in section 3.2 the main contribution still comes from tunneling but the ionization rate has to be modified in order to account for non-adiabatic processes which play a role in that intensity regime. To test this hypothesis simulations are performed that use the exact same parameters as before but incorporate a modified ionization model. The resulting cutoffs can also be seen in figure 5.9. For high intensities, i.e. low Keldysh parameters, the cutoffs from the two models converge to the same value around  $50 U_p$  as in the experiment. As before the ionization only takes place around the peaks of each half-cycle and is not influenced by non-adiabatic processes. For the intensity regime of the nanoparticle measurements the model describes the experimental results well. Down to  $1.0 \times 10^{13} \frac{\text{W}}{\text{cm}^2}$  the relative cutoff is about the same value of  $50 U_p$  in the experiments. The modified model leads to a slightly different ionization probability especially inbetween the laser electric field peak positions. This leads to an earlier generation of electrons and a changed meanfield evolution.

Despite the good agreement in the low intensity range for  $I < 1.0 \times 10^{13} \frac{\text{W}}{\text{cm}^2}$  the relative cutoff drops as in the quasistatic model. Due to the lack of experimental results for very low intensities this trend can neither be confirmed nor definitely disproven. However the measurements hint for an increase of relative cutoff for very weak laser fields which can be explained by the fact that for such large Keldysh parameters a complete multiphoton model has to be included and the tunneling model fails to make any predictions. In the model the electrons are placed at the calculated tunneling exit in a simple picture (similar to figure 2.1b). For low intensities and weak electric fields this exit point is unrealistically far away leading. The electrons do not experience the enhanced near field at their birth positions and show a decreasing relative cutoff. A complete multiphoton model was not implemented yet because the simulation would require a different quantum-mechanical approach. The ionization probabilities do not only depend on the instantaneous fields but also the time evolutions at all probing points around the surface.

Regarding the relative cutoff shown in figure 5.9 the ionization model seems to play a major role in explaining the low intensity behavior. One aspect that was not considered so far is the choice of ionization potential used in our model. The implemented ionization model does not include any bulk properties but just simulates – quasistatic or non-adiabatic – tunneling from single atoms and places the born electron at the calculated tunnel exit position. For silica the difference between atomic and bulk ionization energies is small ( $I_p$  for Si: 8.2 eV and band gap in  $\text{SiO}_2$ : 9 eV). Both values give comparable results but it will be

shown later, that in general the use of bulk parameters will result in better agreement with the experiments. The model uses a modified atom with ionization properties like the bulk material. An improvement could be obtained by choosing a more sophisticated ionization potential by including a band structure and/or the density of states. By ionization or excitation of electrons the population on different energy levels can be changed during the laser pulse which would result in a time-dependent work function.

## 5.5 Results from different materials

To study the role of different material parameters several nanomaterial samples have been investigated. Table 5.1 summarizes all samples used with the properties that were found to have the largest influence on strong-field photoemission, i.e. work function and permittivity (and the resulting field enhancement  $\alpha$ ).

material	diameter	work function $I_p$	permittivity $\epsilon_r$	field enhancement $\alpha$
SiO <sub>2</sub>	80–110 nm	9.00 eV	2.12	1.54
PS	100 nm	4.22 eV	2.50	1.67
ZnS	120 nm	7.50 eV	5.44	2.19
Fe <sub>3</sub> O <sub>4</sub>	110 nm	5.78 eV	5.86	2.24

Table 5.1: Overview over all materials used in this work. The bulk work function was used as ionization potential and the permittivity at 700 nm for the calculation of the electric fields. The permittivities give an estimate of the maximal field enhancement at the poles without taking into account any meanfield effects. For SiO<sub>2</sub> different samples with diameters of 80, 92 and 110 nm diameters were used.

Compared to the other materials SiO<sub>2</sub> has a high work function and the comparably low permittivity leads to comparable low field enhancements. Polystyrene ((C<sub>8</sub>H<sub>8</sub>)<sub>n</sub>, PS) has similar dielectric properties so for those two materials the dipole approximation was used in the simulations since  $\chi = \frac{2\pi r}{\lambda} \ll 1$ . Since PS is much easier to ionize it is an ideal sample for testing the  $I_p$  dependence of the cutoff and test our ionization model in this special case. Both the measurements and the analysis of polystyrene were performed in the same way as for silica with the simulations using the same laser parameters but the material properties of PS.

Comparing PS and SiO<sub>2</sub>, the difference in cutoff energies is noticeable (figure 5.10). Although similar permittivities result in similar field enhancement (PS experiences ~17% higher local intensities than SiO<sub>2</sub>), the photoionization process leads to electrons with about 50% higher energies. Simulations of PS revealed that the relative cutoff energy increases

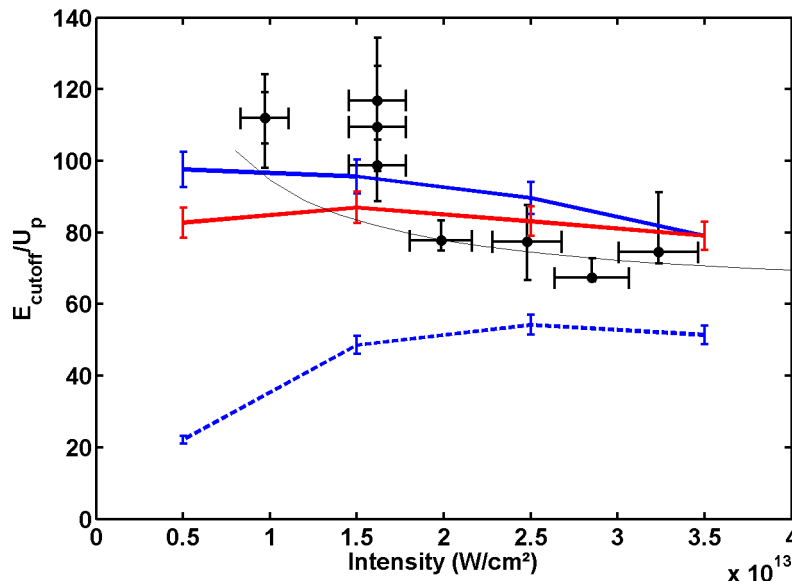


Figure 5.10: Intensity dependent cutoff for 100 nm PS. Black points are showing experimental results while the blue lines corresponds to simulations with the non-adiabatic ionization model for several intensities. A work function of  $I_p = 5.5$  eV resulted in good agreement between experiment and simulation (solid blue) while the atomic work function of  $I_p = 11$  eV shows large deviations (dashed blue line). The red solid line indicates simulations with the quasistatic ionization model ( $I_p = 5.5$  eV). The thin black line indicates the cutoff law according to equation 5.2.

for lower values of  $I_p$  (solid and dashed blue line in figure 5.10 for 5.5 eV and 11 eV, respectively). This effect is in analogy to the non-adiabatic tunneling for low intensities where an relative increase of the ionization rate for lower electric fields leads to earlier emission times of electrons and favorable trajectories.

In the intensity regime shown in figure 5.10 the non-adiabatic tunneling model seems to work very well and can explain the measured cutoff in PS (solid blue line). It should be noted that the implementation of the lowest *atomic* ionization potential of all elements contained in PS (11.26 eV for carbon) drastically underestimates the cutoff (dashed blue line). Since the work function of PS is considerable lower than for SiO<sub>2</sub> the Keldysh parameter is also smaller (in the laser field:  $\gamma \approx 2.3$  and  $\gamma \approx 1.6$  at  $I = 2 \times 10^{13} \frac{\text{W}}{\text{cm}^2}$  for SiO<sub>2</sub> and PS, respectively). The lower  $\gamma$  explains why for PS the quasistatic ionization model (red solid line) gives reasonable results.

In summary the theory not only describes the laser-material interaction for SiO<sub>2</sub> nanoparticles, but also applies to materials with lower work functions. For further evaluation two other samples (see table 5.1) are investigated. Fe<sub>3</sub>O<sub>4</sub> and ZnS yield even higher cutoffs

compared to the other materials. As shown in figure 5.11 the two materials behave similar regarding the cutoff energy which is a result of their similar properties. Since those materials have considerably higher permittivity than  $\text{SiO}_2$  or PS the validity of the dipole approximation has to be checked. It is found that for 100 nm ZnS particles the spatial distribution of electric fields around the nanoparticle can still be approximated by a dipole solution yet the total fields are increased by  $\sim 5\%$ . The particles can still be considered small compared to the wavelength, nevertheless the simulations for those high-permittivity materials are carried out including Mie-theory (up to fourth order) and non-adiabatic tunnel ionization.

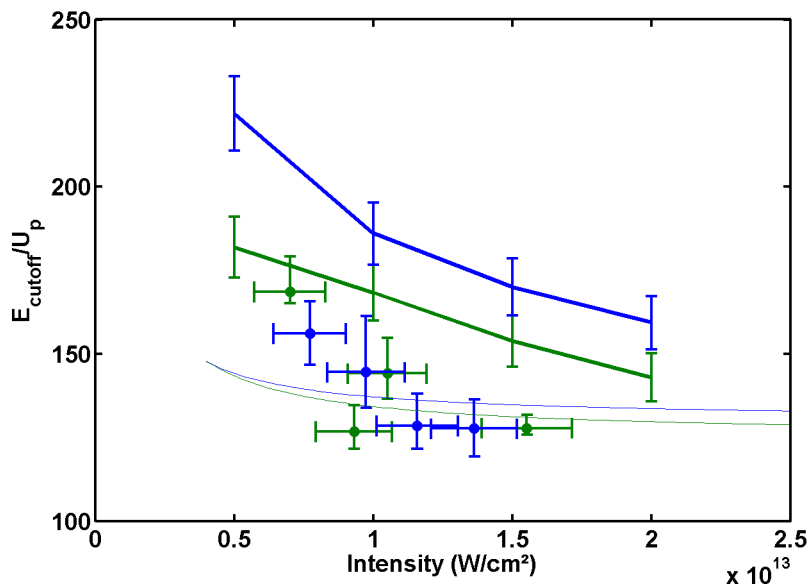


Figure 5.11: Intensity dependent cutoff for 100 nm  $\text{Fe}_3\text{O}_4$  (blue) and 120 nm ZnS (green) nanoparticles. Experimentally the two materials produce the same cutoff within the error bars (orange and blue circles). Simulations (dashed lines) show slightly higher cutoffs than obtained in the experiments, but show the same trend. The thin lines illustrate the cutoff law for gas atoms.

The study of ZnS and  $\text{Fe}_3\text{O}_4$  allows us to investigate the role of material-dependent permittivities in the ionization process. Although the work functions of both materials lie in between  $\text{SiO}_2$  and PS the experimental cutoffs exhibit significantly higher values between  $125 U_p$  and  $170 U_p$  due to the large field enhancements.

The highest experimentally accessible intensity for those materials is lower than for  $\text{SiO}_2$  since the large field enhancement leads to high energy electrons that could not be resolved by the VMI. The lowest intensity is also limited by the number of counts compared to the noise level. Since all samples contained about the same number of particles per volume

solution the lower limit is close to  $1.0 \times 10^{13} \frac{\text{W}}{\text{cm}^2}$ .

As described for  $\text{SiO}_2$  the cutoff law known for gases has to be modified for nanoparticle photoemission. From the comparison with different materials some dependencies can be revealed. The strongest influence is given by the permittivity which affects the field enhancement while the meanfield seems to mostly contribute by a factor. The fact that smaller ionization potentials lead to higher cutoffs can be confirmed in both experiments and simulations but a detailed quantization of this effect is difficult. The measurements of work functions in bulk materials is not as simple as for gases and could in principle be distorted by surface contaminations. Another problem of definite  $I_p$  values is the before-mentioned band structure in solids and the resulting density of states with the corresponding population density.

Therefore it is not straightforward to derive a simple formula for the cutoff in nanoparticle photoemission that depends only on a few parameters because of the many different nonlinear processes taking place. The material properties may lead to different ionization regimes and meanfield effects are complex, but a suitable approach may be derived from the cutoff law for gases. Field enhancement is included with the factor  $\alpha$  and meanfield effects contribute with the factor  $B_{\text{mf}}$ . An approximate cutoff formula for Keldysh parameters not much larger than 1 may then be given by

$$E_c = 10.007 \alpha^2 U_p B_{\text{mf}} + 0.538 I_p. \quad (5.2)$$

The parameter  $B_{\text{mf}}$  is 2.2 for  $\text{SiO}_2$  and PS and 2.6 for  $\text{Fe}_3\text{O}_4$  and ZnS. The resulting curves are shown as thin lines in figures 5.9 to 5.11.

For  $I < 1.5 \times 10^{11} \frac{\text{W}}{\text{cm}^2}$  the total electron yield decreases and the meanfield contributions become negligible. Simulations of that regime suggest an intensity dependent parameter  $B_{\text{mf}}(I)$  varying between 1 for low intensities and 2.2 or 2.6 for high intensities.

## 5.6 Conclusion

The experiments and simulations described here allow us to gain insight into the photoemission and acceleration of electrons on attosecond timescales in and around nanoparticles in strong fields. Isolated nanoparticles open up the possibility to treat the interaction of laser fields with dielectric spheres numerically.

The comparison of simulations and experimental results verifies assumptions in the model, including the influence of scattering events, the electric field distribution around the particle according to Mie theory and the influence of the Keldysh-parameter and the work function on the ionization process.

The experiments in strong fields help in the understanding of processes on a timescale shorter than 1 femtosecond, most importantly the ionization process of solids in strong fields which can neither be simulated easily nor solved analytically. A Keldysh parameter larger than 1 in addition to the non-uniform field distribution around the particles raises the question whether the tunneling or multiphoton regime is valid in the intensity regime of  $1\text{--}5 \times 10^{13} \frac{\text{W}}{\text{cm}^2}$ . Although quasistatic tunnel ionization can be used to simulate the measured electron momentum distributions and CEP dependence, there are indications that the ionization process is different in the low intensity regime. An intensity dependent study of the cutoff energies for several materials suggests that the pure tunneling ionization rate, which applies for high intensities, has to be modified for Keldysh parameters above 1 to a non-adiabatic model suggested by Yudin and Ivanov [26]. After implementing the model in the simulations they show an improved agreement with the experimental results and can explain the obtained cutoff values for Keldysh parameters up to  $\sim 3$ .

The comparison of different materials reveals the influence of the ionization potential on the acceleration of electrons. Smaller ionization potentials lead to higher final energies in both experiment and simulation. Simulations can also confirm the bulk work function as the important value for the ionization process instead of the atomic ionization potential.

Rescattered electrons achieve much higher energies compared to gas photoemission. The main reasons are identified as field enhancement around the dielectric sphere and meanfield effects. The highest relative cutoff energies have been measured for materials with high permittivities like ZnS and  $\text{Fe}_3\text{O}_4$ .

# Chapter 6

## Attosecond streaking on isolated nanoparticles

Attosecond laser pulses trigger the ionization process in a very precise and controllable way which permits us to investigate ultrafast processes like scattering in nanoparticles. The attosecond streaking experiments use the setup described in chapter 4.3 and their results are compared to a theoretical model as described in chapter 3.3.

### 6.1 Methods

The spectra of streaked electrons are recorded by a TOF spectrometer in the polarization direction of the IR pulse under a full opening angle of  $45^\circ$ . Each scan includes a measurement of both background gas and nanoparticles with a delay step size between 80 as and 300 as. Negative delays imply that the XUV pulse arrives before the VIS/IR pulse and vice versa for positive delays. Background measurements were recorded with the whole nanosource setup running with ethanol only which was used as a solvent for the nanoparticle samples. This way all conditions besides the nonparticle sample being present or not are unchanged between the nanoparticle and the reference scan. Neon was used as a carrier gas due to its high ionization potential. The TOF spectrometer is calibrated in a similar way as described in chapter 5.1 by analyzing the ATI peak positions in the electron spectrum from IR-ionized xenon gas.

The cutoff energy of the XUV pulses is at  $\sim 37$  eV (figure 6.1a) so due to the work functions of 9 eV for  $\text{SiO}_2$  and 10.6 eV for ethanol the resulting cutoffs in the electron spectra are at  $\sim 28$  eV and  $\sim 26$  eV, respectively (without streaking). The raw spectra averaged over all delays (red) are shown in figure 6.1b (solid lines for  $\text{SiO}_2$  and dashed lines for ethanol). At low energies they contain an ATI-contribution from IR-photoemission and a

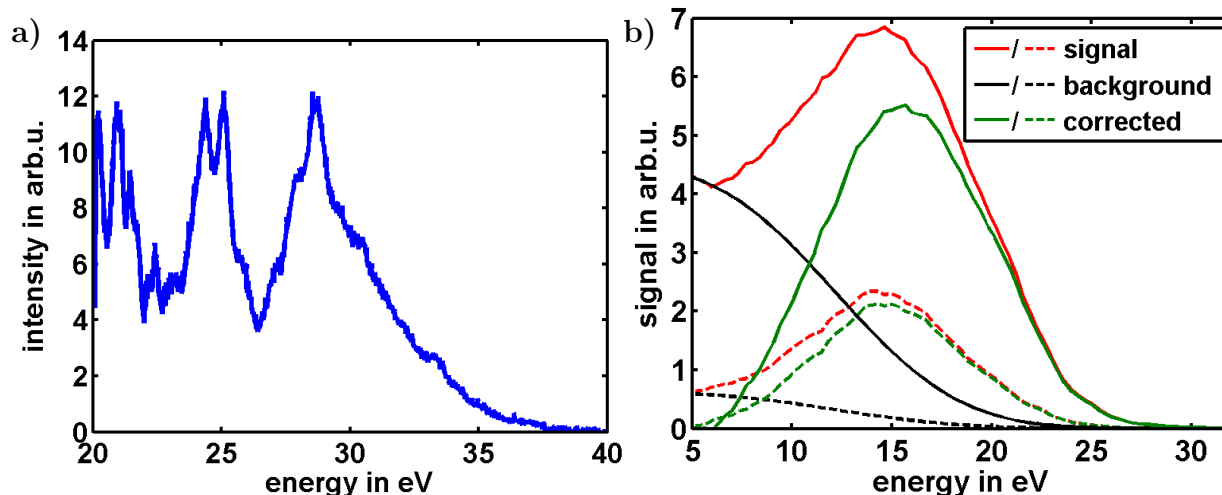


Figure 6.1: a) XUV spectrum. The spectrum is recorded behind the experimental chamber with an MCP and has a cutoff of  $\sim 37$  eV. b) Electron spectra recorded with the TOF spectrometer. The spectra are recorded in polarization direction for both nanoparticles (solid lines) and reference scans in ethanol (dashed lines). The raw spectra (red) are averaged over all delays and show a cutoff of  $\sim 26$  eV for the reference scan and  $\sim 28$  eV for nanoparticles. The background function is assumed to be constant for all delay steps and shown in black. The resulting spectrum after background subtraction is used for further analysis (green).

delay independent contribution from the low energy part of the XUV pulse. To separate those parts from the delay dependent streaking signal the empirical function

$$A \cdot \exp\left(\left(\frac{E}{15 \text{ eV}}\right)^3\right) \quad (6.1)$$

is subtracted (black lines).  $A$  is equal to the signal at low energies assuming zero streaking contribution in that energy range. The width of 15 eV expresses the width of the IR-signal and – in combination with the power of 3 – ensures that any high energy regions which are of interest in the analysis are not affected by the background subtraction procedure. The background is subtracted for all delays and results in the spectra used for further analysis (green).

Reference and nanoparticle (figure 6.2a and 6.2c) scan do not perfectly overlap on the delay axis because the stabilization mechanism described in chapter 4.3 could not eliminate thermal drifts on very long timescales. However the the periodicities in both scans are the same. To compensate for the shift the two measurements are overlapped by applying a least-square fitting routine in the region of 7–17 eV. This is done by minimizing the

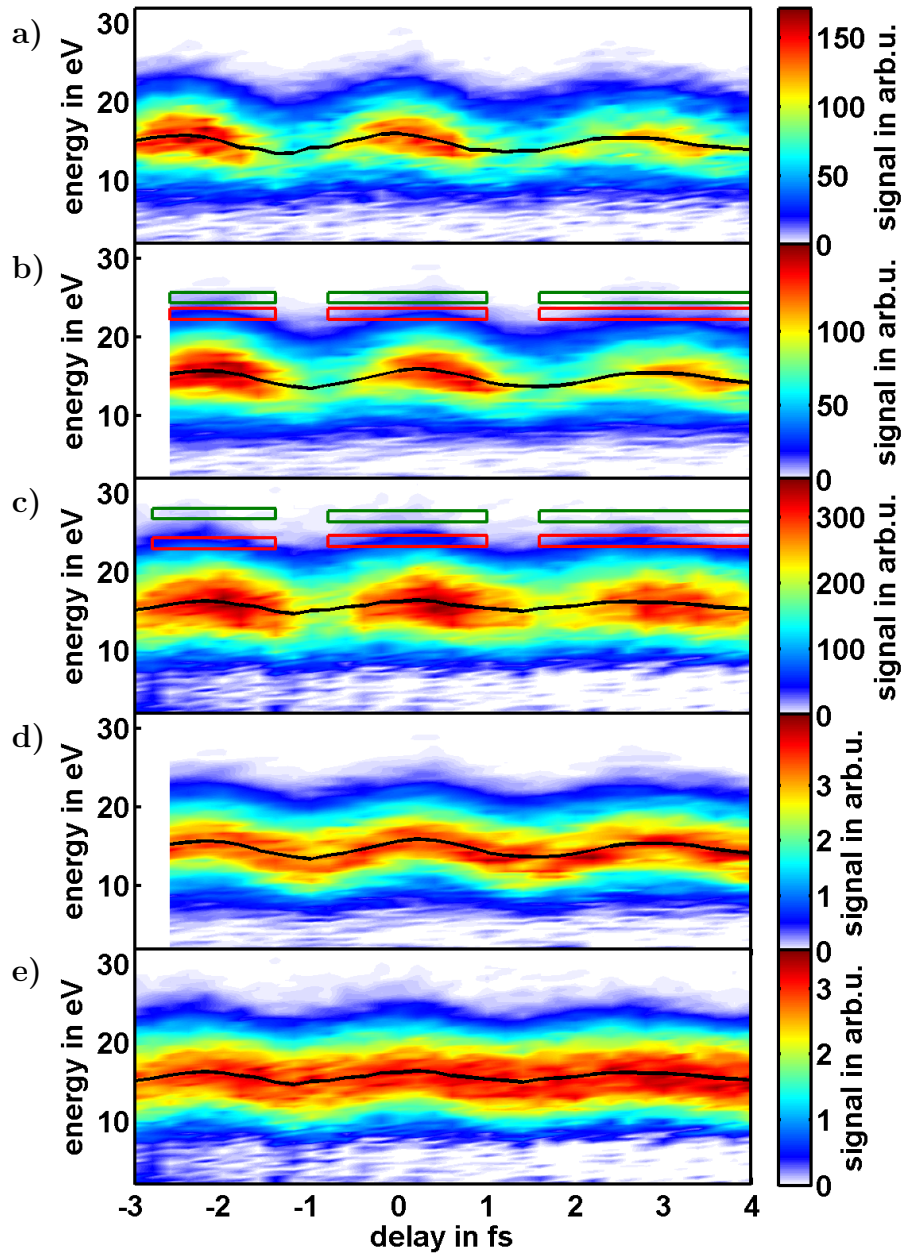


Figure 6.2: Streaking traces. Each electron spectrum is recorded for a certain delay between the VIS/IR pulse and the XUV pulse. The ATI background is subtracted as given by equation 6.1. The black solid line shows an approximation of the vector potential (see text for description). The red and green intervals indicate the energy ranges that are used for a closer analysis of the temporal shape of the streaking trace. a) Reference scan in ethanol. b) Reference scan shifted by +0.5 fs. The fitting procedure is described in the text. c) Scan of 90 nm SiO<sub>2</sub> nanoparticles under same conditions as in a). d) Shifted and normalized reference scan. e) Normalized nanoparticle scan.

following sum

$$f(\Delta) = \sum_{t=-2 \text{ as}}^{3.5 \text{ as}} \sum_{E=7 \text{ eV}}^{17 \text{ eV}} (S_{\text{nano}}(t, E) - 2 \cdot S_{\text{ref}}(t - \Delta, E))^2. \quad (6.2)$$

The factor 2 is compensates the lower count rate in the reference scan. The retrieved  $\Delta$  is +0.5 fs in the shown measurement in figure 6.2a and is used to shift the reference scan with respect to the nanoparticle scan.

To account for changes in XUV pulse energy during a measurement the data can be normalized. Normalization is done by scaling all spectra in order to have the same total number of counts for each delay step. The normalized streaking traces for reference and nanoparticle scan are shown in figure 6.2d) and e).

the traces so obtained for ethanol and SiO<sub>2</sub> nanoparticles appear similar in terms of oscillation period and amplitude. In order to reveal important differences between the two measurements and thereby gain insight into the field driven dynamics, a more detailed analysis is performed. The cutoff in the gas streaking measurement is about 28 eV while the streaking for nanoparticles leads to a broader spectrum and a higher cutoff of about 30 eV taking streaking into account.

The reference scan in ethanol is used for retrieving the most important laser parameters. For each delay step the spectrum is fitted by a Gaussian function and the peak of this Gaussian is taken as an approximation of the vector potential (solid black line). This retrieved curve gives a rough estimate for the pulse length ( $\sim 6$  fs) and the carrier-envelope phase which is used in simulations of the streaking experiments. Furthermore the oscillation period is determined as 2.6 fs (equivalent to a central wavelength of  $\lambda \approx 790$  nm) and  $U_p$  is calculated from the initial and final kinetic energies  $W_0$  and  $W_f$  by

$$W_f \approx W_0 + 2U_p \sin^2(\omega_L t + \phi_0) + \sqrt{8W_0 U_p} \sin(\omega_L t + \phi_0) \quad (6.3)$$

as described in [36] in more detail. The VIS/IR intensity is extracted from the ponderomotive potential as  $I \approx 2 \times 10^{11} \frac{\text{W}}{\text{cm}^2}$ . This value is much lower than the estimation from power measurements and geometrical considerations. this increases the error bars of the intensity determination but has no large influence on the results of our analysis.

## 6.2 Experimental results from SiO<sub>2</sub> streaking

Compared to photoemission in intense few-cycle pulses (chapter 5) the XUV pulse provides electrons with an exact defined birth time and energy. The moment of birth can be

controlled by the delay and the initial energy is given by the XUV spectrum. The initial energy above  $\sim 10$  eV results in a totally different kind of trajectories after ionization. The electrons are ionized in a layer under the surface with a depth of up to 1 nm [27]. Usually this is the only moment when scattering in the nanoparticle can happen because after leaving the particle the typical velocities are larger than induced changes by the VIS/IR field. Since the energy changes from streaking are below 2 eV (see equation 6.3 or figure 6.2) the former mentioned rescattering process can be excluded for electrons in the region of interest at  $\sim 15$  eV and above. However those very first scattering events after ionization taking place in a thin layer right under the surface are of great importance and as we will elaborate possess distinct signatures that allow a comprehensive analysis.

The signatures of nanoparticle streaking can only be identified when separating the nanoparticle signal from background gas. At low energies the signal is a mixture of neon, ethanol, SiO<sub>2</sub> and other gases in the experimental chamber which are almost impossible to distinguish from each other. Only for high energies close to the cutoff the spectrum can be safely assumed to originate only from nanoparticles due to the higher ionization potentials for ethanol and neon. As indicated in figure 6.2 several energy intervals of about 1.3 eV width are chosen for each peak in the streaking trace and compared to the lower energy region around 15 eV represented by the black line in figure 6.2. This line follows approximately the vector potential of the VIS/IR field. All chosen intervals are fitted by sinusoidal functions (solid lines in figure 6.3) to the measured signals (filled dots). The same has been done using Gaussian fit functions (not shown here) and the resulting peak positions for each fit are the same as for sinusoidal fits in the limit of the obtained error bars. The retrieved fits allow a comparison of the streaking signal at different energies between reference and nanoparticle scan.

In the case of gas streaking (figure 6.3a) the maximal signal for each energy region is reached at the same delay. The final energy is mainly determined by the birthtime in the continuum when the electron starts to quiver in the electric field. This behavior however is the same for all final energies and does not depend on the initial energy.

In contrast to gas streaking electrons from nanoparticles show a different temporal dependence close to the cutoff compared to low energy electrons. The black line is the peak line of the streaking trace which is used as a reference point for further analysis. The green line at low energies at about 24 eV is shifted by some tens of attoseconds while the signal at energies around 27 eV (red curve) is displaced by  $\sim 200$  as (figure 6.3b). The exact energies are adapted to the height of the cutoff for each peak (see figure 6.2), e.g. for the third peak intervals with slightly lower energies are chosen.

In free space electrons are expected to gain the highest energies when released at the

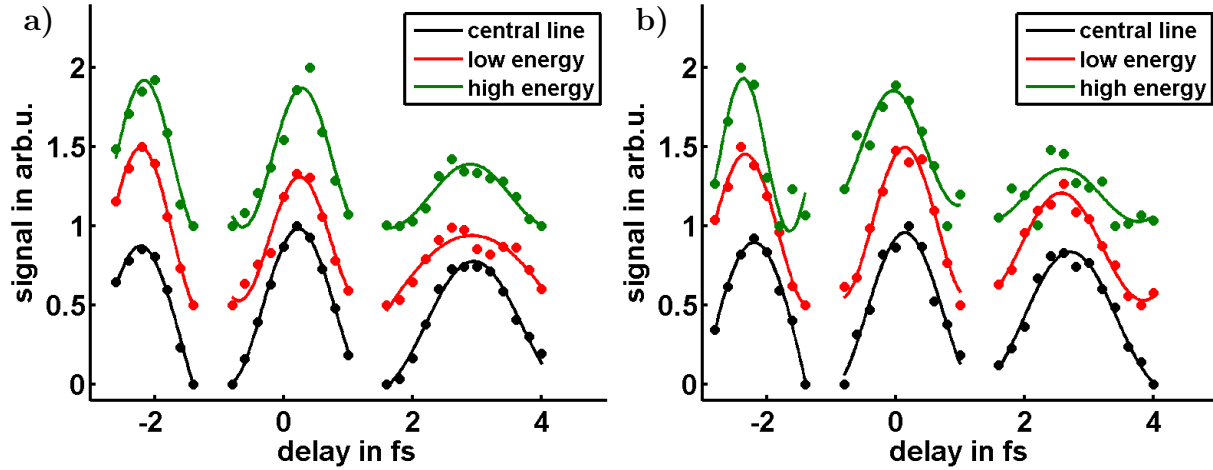


Figure 6.3: Signal of streaking traces for several energies. a) Reference scan with ethanol (and other gases). The black points represent the vector potential as described in section 6.1 (proportional to energy). The green and red points depict the signal in the lower and higher energy part as illustrated in figure 6.2 – averaged over 5 energy steps and scaled arbitrarily (proportional to electron signal). All traces are fitted by a sinusoidal function which is shown as a solid line. b) For the  $\text{SiO}_2$  measurement the same color coding is used and the fits are determined the same way as in a).

maximum of the vector potential while for nanoparticles this moment seems to be shifted in time for certain energies, i.e. the electron has to be ionized earlier in order to gain the same final energy. The main goal of the following analysis is to identify the physical processes that lead to the energy dependent shift of the signal.

First of all an analysis of several different scans is performed to investigate the influence of some properties of the experimental setup on the shift in the streaking trace. For example the thickness of the Al-filter after HHG generation is varied which changes the chirp of the XUV pulse. In the limits of the error bars no significant influence on the observed shift could be identified. In total, 9 scans from several weeks of measurements with varying XUV spectra (about 1 eV variation in cutoff energy) are analyzed in detail and compared to reference scans with ethanol, neon and other gases. For a complete understanding not only 2 energy intervals as indicated above are chosen but a whole series starting from the central region up to the cutoff at about 28 eV.

For each scan all cycles (up to 4) are evaluated for all indicated energy intervals. Figure 6.4a contains the average of 9 different measurements (black points). They are recorded during two campaigns that used two different prevacuum pumps attached to the experimental chamber. A more powerful pump resulted in a lower background pressure, less counts from background gas and eventually a slightly larger shift of the streaking trace.

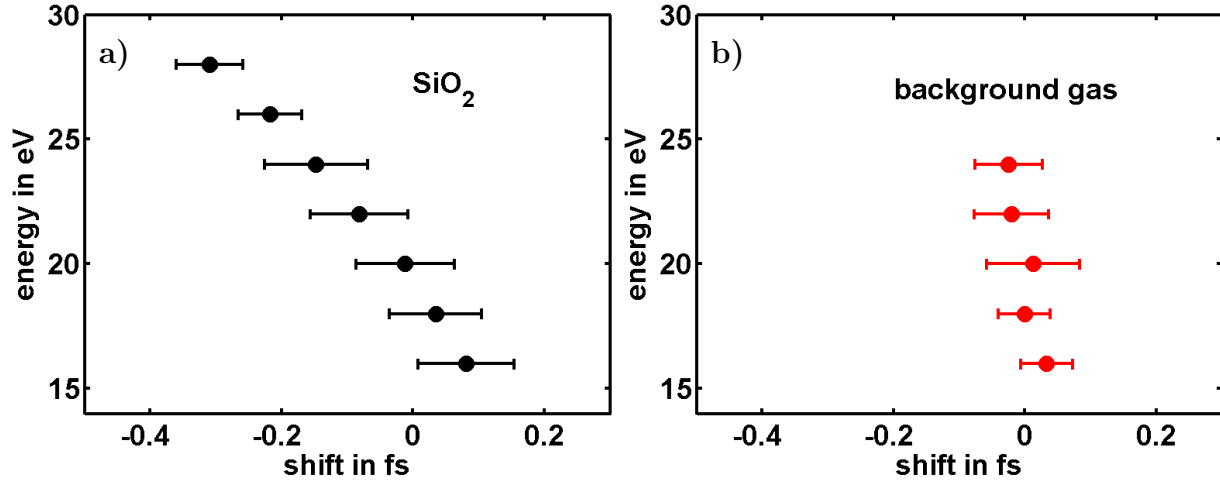


Figure 6.4: Shift in streaking traces for several energies. a) All shifts for the selected energies are determined as indicated in figure 6.3 with respect to the central line used as the vector potential. Each black point is the mean value of 9 measurements under varying conditions and the error bars correspond to the standard deviation of the 9 data points. Each streaking measurement includes up to 4 peaks by its own. The total shift over the whole interval of 12 eV amounts to  $\sim 400$  as. b) The same methods applied to three reference scans in gas which are shown as red points. The highest evaluated energy is only 24 eV because of the lower cutoff in gas streaking. This plot does not show any significant energy-dependent shifts for ethanol within the experimental error bars.

Despite variations in the exact amount of shift all nanoparticle measurements show a delayed behavior of high energy electrons with respect to low energies. All delays in this figure refer to the fitted central line in each scan as the vector potential. However in the case of nanoparticle measurements it is not obvious that this line corresponds to the real vector potential of the driving laser field because in this energy region well below the cutoff the signal is a mixture of background gas and nanoparticle streaking. Nevertheless it serves as a robust indicator and reproducible reference for the low energy region. As a conclusion it is challenging to experimentally determine the absolute shift with respect to the laser field but the comparison of several energy regions is possible within one scan and gives reliable numbers for the *relative* shift. The mean values of all scans are shown as the larger black points and indicate a clear trend towards earlier delays for higher energies.

The exact same methods were used for scans in ethanol as a reference. The retrieved delay positions result in the shown red points which are also averaged over all obtained scans. Due to the lower cutoff the highest possible energy that is evaluated is 4 eV lower than for nanoparticles. Gas scans show no significant shift of the high energy electrons (24 eV) with respect to the signal from low energies (15 eV). Since our analysis only relies on

*relative* shifts the gas streaking measurement defines the shift zero in figures 6.4a and 6.4b. The gas streaking results agree well with theoretical expectations and confirms that the experimental setup allows to identify unique signatures from nanoparticles overlying the background gas. This comprises the very first realization of streaking from nanoparticles.

The electron spectra for very large and very small delays where XUV and IR do not overlap show no significant difference between background gas and nanoparticle scan. This indicates that meanfield effects from IR-photoemission are negligible for attosecond streaking. For very large delays the photoemitted electrons from the VIS/IR pulse lead to a charged nanoparticle and a trapping potential. In case of a large number of electrons these fields would influence the XUV-electrons ionized afterwards. Such a change of the spectra is however not observed.

### 6.3 Comparison of experimental results with simulations

In contrast to experiments, simulations can directly resolve the different scattering processes that take place during streaking experiments on nanoparticles. The model described in chapter 3 uses the laser parameters obtained from the streaking traces in figure 6.2a as input parameters ( $\lambda = 780$  nm,  $\sigma = 6$  fs,  $I = 2 \times 10^{11} \frac{\text{W}}{\text{cm}^2}$ ). For a first test, the permittivity was set to  $\epsilon = 1$  and the ionization potential to  $I_p = 10.6$  eV to simulate the streaking of ethanol.

Figure 6.5 includes all electrons emitted in positive  $z$ -direction under a full opening angle of  $45^\circ$ . An initial kinetic energy of the XUV electrons of  $27 \text{ eV} - 10.6 \text{ eV} = 16.4 \text{ eV}$  and a streaking amplitude of about  $1.7 \text{ eV}$  according to equation 6.3 is expected. The idealized streaking trace is indicated by the scaled vector potential (black line). For gas no shift as a function of the energy region is observed.

The IR pulses have the same parameters in the nanoparticle simulations as for the ethanol simulation. The target is changed by choosing the correct properties of the  $\text{SiO}_2$  particles ( $d = 90$  nm, dipole solution due to small size,  $\epsilon = 2.12$ ,  $I_p = 9$  eV). Inelastic scattering was turned on, but figures 6.6a-c show only electrons that had zero *inelastic* scattering events in order to understand the exact influence of single *elastic* scattering events. They show the resulting streaking traces for exactly 0, 1 and 2 elastic scattering events, respectively. Only 14% of all electron perform no inelastic scattering event and out of those 40%, 21% and 13% perform 0, 1 and 2 elastic scattering events, respectively. So figure 6.6a for example contains only 5.7% out of all electrons in the simulation. Ex-

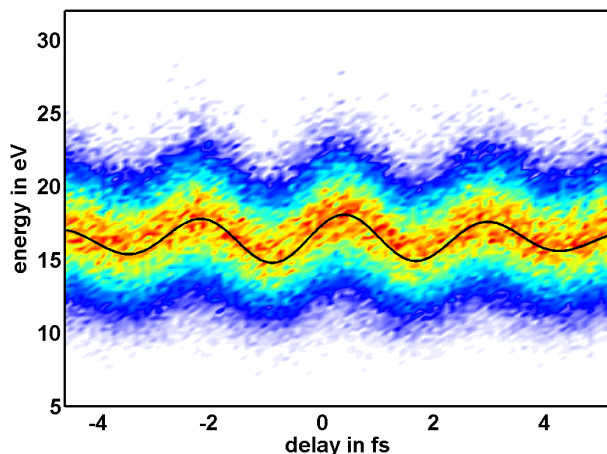


Figure 6.5: Simulation of streaking in ethanol. The parameters of the laser pulses are extracted from the streaking traces in figure 6.2. The central wavelength of the VIS/IR-pulse is 778 nm with an intensity of  $I = 2.2 \times 10^{11} \frac{\text{W}}{\text{cm}^2}$  and the XUV pulse is centered around 27 eV with a width of 5 eV. For ethanol the ionization potential of  $I_p = 10.6$  eV is used and  $\epsilon$  is set to 1. For the final analysis all electrons under a full opening angle of  $45^\circ$  are evaluated for all delays. The black solid line shows the vector potential of the driving laser field which is shifted according to  $\hbar\omega_L - I_p$  and scaled according to equations 6.3.

periments and simulations show the same differences in the electron spectra compared to gas streaking. The photoelectrons have higher initial kinetic energies due to a lower  $I_p$ , resulting in a shifted streaking trace in energy. They also experience a larger streaking amplitude due to a larger  $U_p$  (see also equation 6.3) because of field enhancement near the pole of the nanoparticle in polarization and detection direction. In the experiment quasielastic scattering also might occur when electrons couple to the thermal movements of the atoms in the particle. On the timescale of few femtoseconds only single collisions with some tens of meV at room temperature can not affect the streaking traces drastically. They are not considered in the simulation model.

The comparison of different numbers of scattering events reveals the following dependence: A higher number of collisions shifts the streaking trace to "the left", i.e. to delays where the XUV pulse arrives earlier than the VIS/IR pulse. A shift in delay corresponds to an earlier birth time in the particle. While electrons born close to the surface of the particle directly propagate in the electric field, electrons born at larger depths take some time to escape from the particle. In other words, electrons in larger depths have to be ionized by an earlier XUV-pulse in order to leave the particle at the same time as a surface electron. Since electrons that are born below the surface travel a larger distance in the nanoparticle material, they are more likely to undergo elastic scattering. This principle

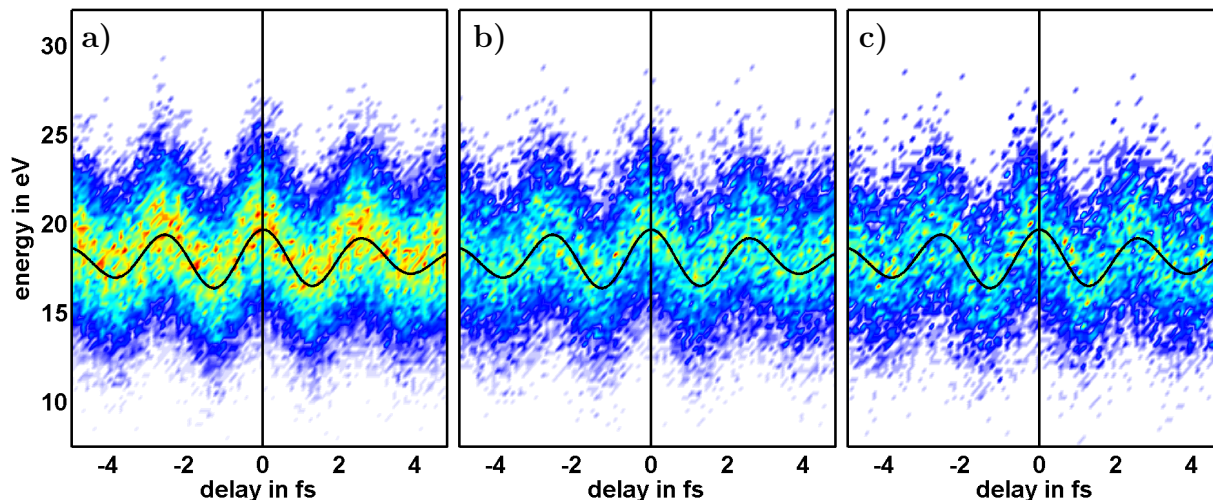


Figure 6.6: Simulation of streaking of 90 nm  $\text{SiO}_2$  nanoparticles for different numbers of elastic collisions. The laser parameters for this simulation are the same as for the ethanol scan. The parameters for the  $\text{SiO}_2$  nanoparticle are taken from the literature [22, 24]. The elastic mean free path is energy dependent as described before (2–3 Å) and  $I_p = 9$  eV. Inelastic scattering was turned on but all plots show electrons with zero inelastic scattering events to inspect the effects of elastic scattering. a) 0 elastic collisions, b) 1 elastic collision and c) 2 elastic collisions.

provides the link between a shift in time and the collision process. Since elastic scattering happens isotropically, it can be seen as a completely new ionization process delayed by the time an electron takes to travel one elastic mean free path.

A systematic analysis of streaking traces shown in figure 6.6 was done for 0 to 4 elastic collisions. The shifts are evaluated in an energy region from 20 to 26 eV and compared to the vector potential (lines in figure 6.7a). This temporal reference point is directly accessible in simulations, as opposed to the analysis of experimental data where the vector potential can only be estimated by a fit. Each colored line corresponds to a certain number of collisions as indicated at the top. The points in the upper part show the shift for the integrated energy interval 20–26 eV. On average one elastic scattering event causes a delay of 60 as which is equivalent to an elastic mean free path of 1.6 Å. This value is lower than the implemented mean free path because it is reduced by the influence of inelastic scattering.

When shutting off inelastic scattering completely and adding the signal from electrons with all possible numbers of elastic scattering events (0, 1, 2, ...), the resulting streaking trace is washed out completely on the delay axis (figure 6.7b). Only in the cutoff region a certain oscillation can be detected which is shifted with respect to the vector potential.

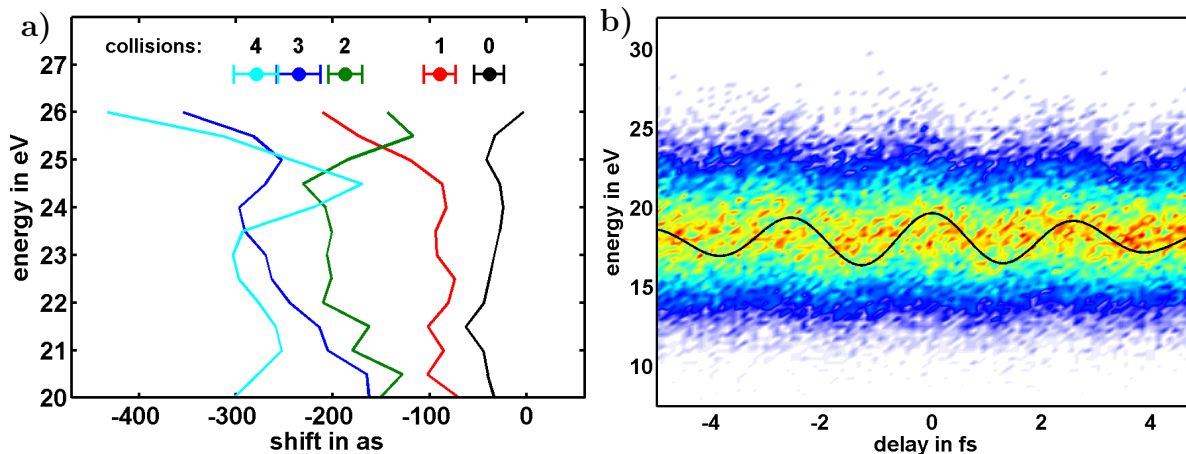


Figure 6.7: a) Shift induced by electron collisions. The streaking traces shown in figure 6.6 are taken and evaluated by the same fitting procedures as the experimental data for an energy region from 20 to 26 eV (traces for 3 and 4 collisions are not shown in figure 6.6). The analysis is done for each number of elastic scattering events separately as indicated by the number at the top. All shifts are determined with respect to the vector potential. The points above the lines show the shift in the region integrated over 20–26 eV (weighted average by signal strength). b) Streaking trace for 90 nm SiO<sub>2</sub> nanoparticles without implementation of inelastic scattering. The simulation shows all electrons, including all possible numbers of elastic scattering events.

Without inelastic scattering electrons can be ionized and stay inside the nanoparticle for a long time by scattering with several atoms. As mentioned earlier those scattering events act as a reset of birth time so the electron finally leaves the particle at a random moment which is independent of the original birth time. Since the birth time – determined by the delay – and the escape time – determining the final energy – are not correlated anymore, the streaking trace is more or less independent of the delay and shows not temporal structure.

Which process changes this picture and leads to clearly defined streaking traces? Figure 6.8 shows a simulation with inelastic scattering turned on. Figure 6.8a) and 6.8b) contain all electrons with no and exactly one inelastic scattering event, respectively. The simulations use a scattering model derived from atomic scattering theory as described by equation 3.2. We assume that every electron that undergoes one inelastic scattering event loses an energy of  $I_p$ . The typical energy gained due to acceleration in the laser field is much lower ( $<2$  eV) than the ionization potential (9 eV), so after undergoing inelastic collisions electrons will show up in the streaking trace at much lower energies. Therefore inelastic scattering has a "cleaning" effect. The previously described washing out of the streaking trace due to a high number of elastic collisions (see figure 6.7b) can not happen anymore because at the same time there is a large probability for inelastic scattering. Both scat-

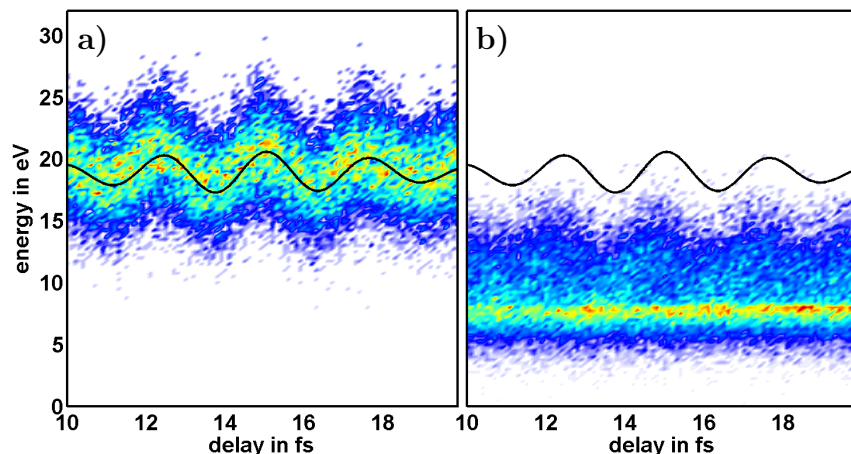


Figure 6.8: Streaking traces of 90 nm  $\text{SiO}_2$  nanoparticles with inelastic scattering turned on to investigate its effect on the energy electron distribution. For this simulation the same laser parameters as before are used. Both figures contain all possible numbers of *elastic* collisions. a) 0 inelastic scattering events b) 1 inelastic scattering event.

tering probabilities are correlated since they depend on the total distance traveled inside the particle. Electrons undergoing many elastic collisions cannot wash out the trace by exhibiting a large delay, since they most likely will undergo an inelastic collision and thus disappear from the relevant energy spectrum. In figure 6.8a almost 50% of all electrons did not experience any elastic collision at all – the other part underwent a low number of collisions. The low number of scattering events preserves the correlation between delay and final energy.

A simulation including all possible scattering processes included gives the best approximation of experimental results. Figure 6.9 shows the spectra from all electrons in the direction of the TOF-spectrometer independent of the number of scattering events. The high energy region is mostly influenced by electrons with a few elastic but no inelastic scattering events while the low energies regions are populated with electrons after inelastic scatterings. The overall shape in figure 6.9a resembles the experimental results but in order to understand the influence of scattering a closer look at the shift of the streaking trace is necessary.

The analysis of figure 6.9a reveals a shift in the high energy region of about 100 as with respect to vector potential and an average of 1.8 elastic collisions in this region of interest. This agrees well with the analysis from figure 6.7a. This value however does not agree with the numbers obtained in the experiment where the shift is  $\sim 300$  as. For a second simulation the probability for inelastic scattering is decreased by a factor of 5 (figure 6.9b). This way the electrons are able to do more elastic scatterings, stay inside the particle for a

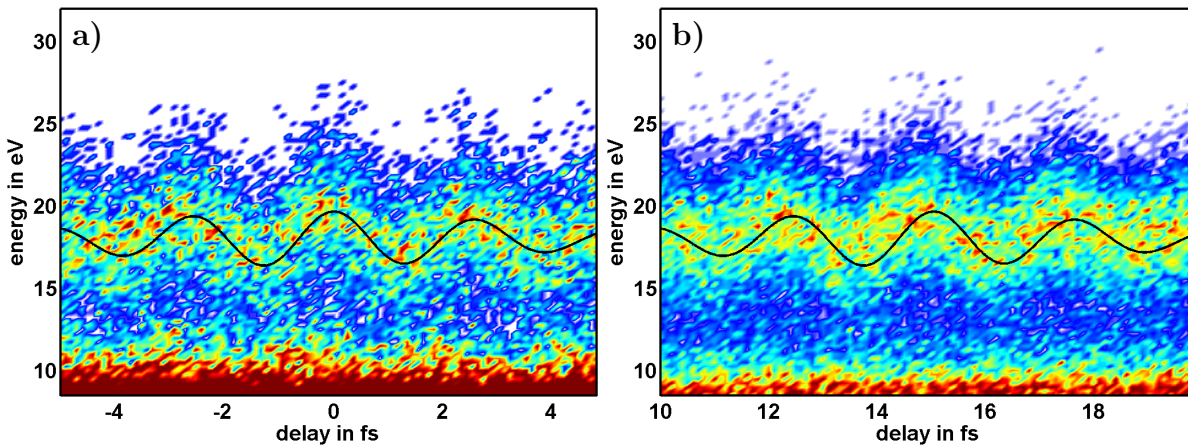


Figure 6.9: Streaking traces with elastic and inelastic scattering turned on. All electrons with several inelastic scattering events show up at the very low energy region. a) The inelastic scattering probability from the universal curve was used leading to a shift of about 100 as. The mean value of elastic scattering events in the high energy region is about 1.8. b) All parameters are the same as in a) except for the inelastic scattering probability, which was reduced by a factor of 5. Now the shift close to the cutoff increased to about 300 as and the mean value of elastic scattering events went up to 5.9.

longer time and lead to a larger shift in the high energy region. In this case the electrons approximately scatter elastically 5.9 times which introduces a shift of  $\sim 350$  as, close to the experimentally obtained value.

In general it is however not straightforward to compare the experimental to the simulated data because in the experiment the whole streaking trace is a mixture of the signals from nanoparticles and background gas. Only electrons with very high energies originate purely from nanoparticles and are used for further analysis. The comparison of shifts in experiments and simulations reveal an average of 5.9 elastic collisions events before electrons scatter inelastically and fall out of the streaking trace. Furthermore our simulations suggest a drastically longer inelastic mean free path than derived from atomic cross sections. More detailed studies including simulations with more sophisticated XUV photoemission and scattering models are currently performed in the group of Prof. Dr. Thomas Fennel at the Universität Rostock.

## 6.4 Conclusion

This chapter shows the first realization of streaking on isolated nanoparticles.  $\text{SiO}_2$  nanoparticles are hit by XUV pulses and streaked by a few-cycle VIS/IR-pulse. The electron spectra are recorded by a TOF spectrometer for certain delays between the two laser pulses. A

careful analysis of the measured streaking traces shows a shift of the high energy signatures in negative delay direction. The shift of  $\sim 300$  as can not be seen in reference scans and supports the assumption that this part of the signal originates from ionized nanoparticles.

Simulations reveal the influence of elastic and inelastic scattering processes on the streaking trace and identify those effects in the experimental data. In general, elastic scattering processes occurring before electrons leave the nanoparticle lead to a shift of the delay. The final shift in the measurement is always an equilibrium between the number of elastic collisions and one inelastic scattering event. Inelastic scattering lowers the energy of the electron and thereby sets an upper limit to the maximum shift in the high energy region.

Simulations could reproduce this behavior and separate several influences, especially distinguishing between elastic and inelastic scattering. It was shown that elastic scattering correlates with the shift observed in the experiment. One elastic scattering event leads to an average shift of  $\sim 60$  as.

The simulations provide insight in the timings of those scattering processes and suggest that the photoemitted electrons born beneath the particle surface undergo about 6 collisions before losing energy by an inelastic scattering event. For good agreement with the experiment the inelastic scattering probability has to be chosen much lower than expected. The value of 6 elastic collisions assumes that the experiment can clearly assign the high energy signal to nanoparticles and is not influenced by a gas signal. We also made the assumption that the low energy region corresponds to the signal from gas atoms and is an indicator for the vector potential. When investigating very long inelastic mean free paths the emission depth of the XUV electrons plays a role and might be the limiting factor of the delay at high energies.

# Chapter 7

## Conclusion and outlook

The objective of this work was to study the photoionization process from isolated nanoparticles in detail. In the first part, the electron emission in strong fields as a function of the CE phase of the laser pulses was investigated. In the second part, the photoemission process was triggered on a attosecond timescale by an XUV pulse. Both experiments gave insight into very fundamental processes, i.e. the ionization process in strong laser fields and scattering processes in solids.

Based on those experiments a cutoff formula for rescattered electrons similar to the cutoff in gases is proposed which includes meanfield contributions and field enhancements. The influence of the bulk work function as well as the material permittivity on the energy of rescattered electrons is investigated. The cutoff energy depends on those parameters and can be modeled with the M<sup>3</sup>C-Code used in this work. The ionization mechanism in intermediate Keldysh regimes is understood and can be treated numerically. Both photoemission in strong IR fields and attosecond streaking deal with the effects of scattering in solids. Attosecond measurements provide the possibility to have a look at the scattering times and mean free pathes of electrons. Even without encountering such ultrafast processes in everyday life we are able to understand the driving mechanisms like electric fields provided by laser pulses. This helps us to improve our understanding of nature and hopefully allows us to control electronic motion on the attosecond timescale.

Equation 5.2 has some uncertainty but the model implemented in this work could be improved by measurements at intensities below  $10^{13} \frac{\text{W}}{\text{cm}^2}$ . This could be achieved by an improvement of some of the experimental parameters like higher nanoparticle concentration in the focus, higher repetition rate or lower noise level. Implementing a single-shot intensity-tagging would allow us to evaluate the measurement not only at the peak intensity but also for all intensities around the laser focus – with clear assignment of actual intensity to electron momentum maps shot by shot. The effects of focus averaging can be

avoided.

The regime of higher intensities is accessible by TOF measurements allowing intensities in the regime above  $10^{14} \frac{\text{W}}{\text{cm}^2}$ . This would also allow us to investigate the ionization processes in either metals or a possible optical breakdown in  $\text{SiO}_2$  [37, 38]. Different intensity values between  $2 \times 10^{14} \frac{\text{W}}{\text{cm}^2}$  and  $2 \times 10^{15} \frac{\text{W}}{\text{cm}^2}$  have been proposed for this threshold.

It was shown that with the help of streaking the ionization process can be triggered on a very short timescale. The information retrieved from streaking measurements can be increased by using a VMI setup for detection. The two-dimensional projection of the momentum distribution can be used to separate the nanoparticle signal from the background noise by a histogram as described in chapter 5. The contributions from nanoparticles can be easily separated from other effects. In addition to that it is possible to use the frames with gas signal as an intrinsic calibration of time zero. Furthermore propagation effects of the XUV-pulse in the nanoparticle could be observed.

By combining the two ideas used in this work it would be possible to investigate the ionization process deeply in the non-adiabatic regime and follow all processes in the nanoparticle on an attosecond timescale. An VIS/IR pulse with an intensity slightly below  $10^{13} \frac{\text{W}}{\text{cm}^2}$  could perform the ionization in the non-adiabatic or even multiphoton regime. The streaking trace of XUV electrons is sensitive to meanfield effects and can thereby monitor the ionization process for large Keldysh parameters. For a separation of the streaking signal from ATI background the XUV energies should be higher than 50 eV.

# Bibliography

- [1] Theodore H Maiman. Stimulated optical radiation in ruby. 1960.
- [2] Robert W Boyd. Nonlinear optics. *Nonlinear Optics: Third Edition. By Robert W. Boyd. ISBN 978-0-12-369470-6. Published by Academic Press/Elsevier, Inc. Oxford, UK, 2008.*, 1, 2008.
- [3] Jean-Claude Diels and Wolfgang Rudolph. *Ultrashort laser pulse phenomena*. Academic press, 2006.
- [4] Ahmed H Zewail. Femtochemistry: Atomic-scale dynamics of the chemical bond. *The Journal of Physical Chemistry A*, 104(24):5660–5694, 2000.
- [5] Ferenc Krausz and Mark I Stockman. Attosecond metrology: from electron capture to future signal processing. *Nature Photonics*, 8(3):205–213, 2014.
- [6] Markus Drescher, Michael Hentschel, R Kienberger, Matthias Uiberacker, Vladislav Yakovlev, Armin Scrinzi, Th Westerwalbesloh, U Kleineberg, Ulrich Heinzmann, and Ferenc Krausz. Time-resolved atomic inner-shell spectroscopy. *Nature*, 419(6909):803–807, 2002.
- [7] LV Keldysh. Ionization in the field of a strong electromagnetic wave. *Sov. Phys. JETP*, 20(5):1307–1314, 1965.
- [8] Paul B Corkum. Plasma perspective on strong field multiphoton ionization. *Physical Review Letters*, 71(13):1994, 1993.
- [9] Matthias Uiberacker, Th Uphues, Martin Schultze, Aart J Verhoef, Vladislav Yakovlev, Matthias F Kling, Jens Rauschenberger, Nicolai M Kabachnik, Hartmut Schröder, Matthias Lezius, et al. Attosecond real-time observation of electron tunnelling in atoms. *Nature*, 446(7136):627–632, 2007.

- [10] Daniel D. Hickstein, Franklin Dollar, Jim A. Gaffney, Mark E. Foord, George M. Petrov, Brett B. Palm, K. Ellen Keister, Jennifer L. Ellis, Chengyuan Ding, Stephen B. Libby, Jose L. Jimenez, Henry C. Kapteyn, Margaret M. Murnane, and Wei Xiong. Observation and control of shock waves in individual nanoplasmas. *Phys. Rev. Lett.*, 112:115004, Mar 2014.
- [11] Sergey Zharebtsov, Thomas Fennel, Jürgen Plenge, Egill Antonsson, Irina Znakovskaya, Adrian Wirth, Oliver Herrwerth, Frederik Süßmann, Christian Peltz, Izhar Ahmad, et al. Controlled near-field enhanced electron acceleration from dielectric nanospheres with intense few-cycle laser fields. *Nature Physics*, 7(8):656–662, 2011.
- [12] S Zharebtsov, F Süßmann, C Peltz, J Plenge, KJ Betsch, I Znakovskaya, AS Alnaser, NG Johnson, M Kübel, A Horn, et al. Carrier-envelope phase-tagged imaging of the controlled electron acceleration from sio2 nanospheres in intense few-cycle laser fields. *New Journal of Physics*, 14(7):075010, 2012.
- [13] Kane S Yee. Numerical solution of initial boundary value problems involving maxwells equations. *IEEE Trans. Antennas Propag*, 14(3):302–307, 1966.
- [14] Allen Taflove and Morris E Brodwin. Numerical solution of steady-state electromagnetic scattering problems using the time-dependent maxwell’s equations. *Microwave Theory and Techniques, IEEE Transactions on*, 23(8):623–630, 1975.
- [15] Gustav Mie. Beiträge zur optik trüber medien, speziell kolloidaler metallösungen. *Annalen der physik*, 330(3):377–445, 1908.
- [16] Pierre Agostini, F Fabre, Gérard Mainfray, Guillaume Petite, and N Ko Rahman. Free-free transitions following six-photon ionization of xenon atoms. *Physical Review Letters*, 42:1127–1130, 1979.
- [17] Maxim V Ammosov, Nikolai B Delone, and Vladimir P Krainov. Tunnel ionization of complex atoms and atomic ions in electromagnetic field. In *1986 Quebec Symposium*, pages 138–141. International Society for Optics and Photonics, 1986.
- [18] M Busuladžić, A Gazibegović-Busuladžić, and DB Milošević. High-order above-threshold ionization in a laser field: Influence of the ionization potential on the high-energy cutoff. *Laser physics*, 16(2):289–293, 2006.

- [19] DJ Bradley, B Liddy, and WE Sleat. Direct linear measurement of ultrashort light pulses with a picosecond streak camera. *Optics Communications*, 2(8):391–395, 1971.
- [20] Ferenc Krausz and Misha Ivanov. Attosecond physics. *Reviews of Modern Physics*, 81(1):163, 2009.
- [21] J Itatani, F Quéré, Gennady L Yudin, Misha Yu Ivanov, Ferenc Krausz, and Paul B Corkum. Attosecond streak camera. *Physical review letters*, 88(17):173903–173903, 2002.
- [22] H-J Fitting, E Schreiber, J-Ch Kuhr, and A Von Czarnowski. Attenuation and escape depths of low-energy electron emission. *Journal of Electron Spectroscopy and Related Phenomena*, 119(1):35–47, 2001.
- [23] AP Greeff and HC Swart. Monte carlo simulation of low-energy electron trajectories and energy loss in zns phosphor powders. *Surface and interface analysis*, 31(6):448–456, 2001.
- [24] Wolfgang Lotz. An empirical formula for the electron-impact ionization cross-section. *Zeitschrift für Physik*, 206(2):205–211, 1967.
- [25] Wolfgang Lotz. Electron-impact ionization cross-sections and ionization rate coefficients for atoms and ions. *The Astrophysical Journal Supplement Series*, 14:207, 1967.
- [26] Gennady L Yudin and Misha Yu Ivanov. Nonadiabatic tunnel ionization: looking inside a laser cycle. *Physical Review A*, 64(1):013409, 2001.
- [27] Pierre Jaeglé. Xuv optics. *Coherent Sources of XUV Radiation: Soft X-Ray Lasers and High-Order Harmonic Generation*, pages 23–40, 2006.
- [28] I Ahmad, SA Trushin, Z Major, C Wandt, S Klingebiel, T-J Wang, V Pervak, A Popp, M Siebold, F Krausz, et al. Frontend light source for short-pulse pumped opcpa system. *Applied Physics B*, 97(3):529–536, 2009.
- [29] Joseph Ladislav Wiza. Microchannel plate detectors. *Nuclear Instruments and Methods*, 162(1):587–601, 1979.
- [30] AM Saylor, Tim Rathje, Walter Müller, Klaus Rühle, R Kienberger, and GG Paulus. Precise, real-time, every-single-shot, carrier-envelope phase measurement of ultrashort laser pulses. *Optics letters*, 36(1):1–3, 2011.

- 
- [31] Dan Oron, Yaron Silberberg, Nirit Dudovich, and David M Villeneuve. Efficient polarization gating of high-order harmonic generation by polarization-shaped ultrashort pulses. *Physical Review A*, 72(6):063816, 2005.
- [32] Werner Stöber, Arthur Fink, and Ernst Bohn. Controlled growth of monodisperse silica spheres in the micron size range. *Journal of colloid and interface science*, 26(1):62–69, 1968.
- [33] F Süßmann, S Zherebtsov, J Plenge, Nora G Johnson, M Kübel, AM Sayler, V Mondes, C Graf, E Rühl, GG Paulus, et al. Single-shot velocity-map imaging of attosecond light-field control at kilohertz rate. *Review of Scientific Instruments*, 82(9):093109, 2011.
- [34] V Roudnev and BD Esry. General theory of carrier-envelope phase effects. *Physical review letters*, 99(22):220406, 2007.
- [35] Gerhard G Paulus, Wilhelm Becker, W Nicklich, and Herbert Walther. Rescattering effects in above-threshold ionization: a classical model. *Journal of Physics B: Atomic, Molecular and Optical Physics*, 27(21):L703, 1994.
- [36] Markus Drescher, Michael Hentschel, Reinhard Kienberger, Gabriel Tempea, Christian Spielmann, Georg A Reider, Paul B Corkum, and Ferenc Krausz. X-ray pulses approaching the attosecond frontier. *Science*, 291(5510):1923–1927, 2001.
- [37] T Otobe, K Yabana, and JI Iwata. First-principles calculation of the electron dynamics in crystalline sio<sub>2</sub>. *Journal of Physics: Condensed Matter*, 21(6):064224, 2009.
- [38] Vadym Apalkov and Mark I Stockman. Theory of dielectric nanofilms in strong ultrafast optical fields. *Physical Review B*, 86(16):165118, 2012.

# Acknowledgements

Prof. Matthias Kling deserves special acknowledgements for his great and professional supervision of this work. He always took his time to answer my questions and gave valuable advice. Without his steady encouragement this work would not have been possible. I am also very thankful to Prof. Ferenc Krausz for giving me the opportunity to write this thesis in his group.

Many thanks to Sergey Zherebetsov for his patient help with the setup and many hours in the lab both in Germany and Italy. He supported all experiments with remarkable commitment. I really appreciate Frederik Süßmann's helpful corrections and discussions. He shared a lot of his knowledge and experience. I would like to thank Hui Li for her assistance with the setup, especially the alignment of the fiber. I'm also very grateful to all other group members for many productive and informative group meetings. Lothar Maisenbacher contributed a lot by his corrections of the script.

Special thanks to Francesca Calegari, Andrea Trabattoni and Sunilkumar Anumula for their support. I really appreciate the help of Thomas Fennel and Leannart Seiffert with the theoretical models. Last but not least many thanks to Prof. Eckart Rühl, Prof. Christina Graf, Prof. Matthias Rehahn, Dr. Markus Gallei, Christian Schäfer, Prof. Jinwoo Lee and Minsu Kim for the production of nanoparticles.



# Erklärung

Hiermit erkläre ich, die vorliegende Arbeit selbständig verfasst zu haben und keine anderen als die in der Arbeit angegebenen Quellen und Hilfsmittel benutzt zu haben.

München, den 16.06.2014

Philipp Rupp